Petroleum Science 23 (2026) 5156–5173

Contents lists available at ScienceDirect

Petroleum Science

journal homepage: www.keaipublishing.com/en/journals/petroleum-science

Original Paper

Mechanical characteristics of deep to ultra-deep sandstones: A comparison study based on rock mechanical and hydraulic fracturing experiments

Zi-Xi Jiao [a,b], Hai-Yan Zhu [a,b,*], Peng Zhao [a], Shi-Jie Chen [a,b], Xian-Bo Meng [c], Shou-Wei Zhou [d], Jun Zhou [e]

[a] College of Energy, Chengdu University of Technology, Chengdu, 610059, Sichuan, China
[b] State Key Laboratory of Oil and Gas Reservoir Geology and Exploitation, Chengdu University of Technology, Chengdu, 610059, Sichuan, China
[c] Sinopec Shengli Oilfield Company, Dongying, 257001, Shandong, China
[d] China National Offshore Oil Corporation, Beijing, 100010, China
[e] College of Geophysics, Chengdu University of Technology, Chengdu, 610059, Sichuan, China

A R T I C L E I N F O

Article history:
Received 14 October 2025
Received in revised form
8 December 2025
Accepted 18 March 2026
Available online 20 March 2026

Edited by Min Li

Keywords:
Ultra-deep tight reservoir
Mechanical characteristics
Hydraulic fracture behavior
Brittle–ductile transition
Break-down pressure

A B S T R A C T

Understanding the evolution of sandstone mechanical behavior under high pressure and high temperature (HPHT) is crucial for the efficient development of ultra-deep tight reservoirs. In this study, triaxial compression tests on ultra-deep core samples and true triaxial hydraulic fracturing experiments on 200 mm × 200 mm × 200 mm sandstone cubes were conducted under HPHT conditions. The brittle–ductile transition behavior and fracture initiation and propagation characteristics of rocks in ultra-deep reservoirs were investigated, and four classical break-down models were employed to evaluate break-down pressures under different stress state and temperature conditions. The results show that, at elevated confining pressures and temperatures, ultra-deep rocks undergo a transition from brittle failure dominated by shear cracks to ductile deformation involving numerous microcracks; pre-peak plastic strain increases markedly, and a pronounced post-peak stress plateau appears in the stress–strain curves, indicating a significant enhancement of overall ductility. Under HPHT conditions, breakdown pressure increases and fracture propagation resistance becomes stronger, and hydraulic fractures tend to exhibit an intermittent "initiation–arrest–reinitiation" propagation pattern, which is unfavorable for the development of a complex fracture network. Comparison of model predictions with experimental and field data further demonstrates that, for reservoirs deeper than 5000 m, thermally induced stresses should be incorporated into break-down pressure prediction. Among the four models considered, the T-H-W model exhibits superior physical plausibility and predictive reliability for ultra-deep tight reservoirs. These findings provide important experimental and theoretical support for optimizing hydraulic fracturing design and enhancing stimulation effectiveness in ultra-deep tight formations.

1. Introduction

As global demand for oil and gas continues to grow, deep to ultra-deep tight reservoirs have become increasingly important targets for exploration and development (Li et al., 2022; Yang and Zou, 2022). Lithologies in deep to ultra-deep reservoirs are mainly carbonates, shales, and clastic rocks, with the dominant reservoir type varying significantly among different basins and structural units (Zhang et al., 2024). Among them, sandstone is one of the most representative rock types in deep to ultra-deep tight

* Corresponding author.
E-mail address: zhuhaiyan040129@163.com (H.-Y. Zhu).
Peer review under the responsibility of China University of Petroleum (Beijing).

https://doi.org/10.1016/j.petsci.2026.03.041
1995-8226/

reservoirs and has attracted extensive attention in both fundamental research and engineering practice (Qin et al., 2024; Zhang et al., 2024). In China, tight reservoirs with burial depths greater than 3.5 km are generally classified as deep, whereas those deeper than 4.5 km are regarded as ultra-deep (Jia, 2023; Sun et al., 2025; Qin et al., 2024). Deep to ultra-deep tight reservoirs are characterized by complex geological conditions, with high temperatures (typically >100 °C) and high pressures (typically >105 MPa), which pose major challenges for exploration and production (Lei et al., 2021; Qin et al., 2024). Large-scale exploration and development of deep to ultra-deep reservoirs have already been achieved in the Tarim Basin and Sichuan Basin in China, as well as in the Rub' al Khali Basin in the Middle East, accompanied by substantial advances in well logging (Wang et al., 2022; Ma et al., 2024), drilling and completion (Guo et al., 2018; Yang et al., 2025), and reservoir stimulation technologies (Liu et al., 2023a; Yong et al., 2025). However, compared with engineering practice, systematic studies on the rock mechanical properties of deep to ultra-deep formations and their evolution remain clearly insufficient, and have become one of the key factors constraining the efficient development of deep to ultra-deep tight reservoirs.

The rock mechanical behavior of deep to ultra-deep formations plays a critical role in geological characterization, drilling safety, and hydraulic fracturing performance, among which the brittle–ductile transition is a key mechanism controlling rock mechanical properties (Davarpanah et al., 2023; Li et al., 2026; Zha et al., 2025). Limited by early drilling technology and laboratory loading capabilities, many previous studies were conducted on outcrops or cores from shallow to medium reservoirs, and the effects of confining pressure and temperature on brittle–ductile transition were examined mainly under relatively low confining pressures (Chen et al., 2025a; Zhang et al., 2015a). These studies showed that, with increasing confining pressure, rock failure mode (Segall and Simpson, 1986; Xie et al., 2021), stress–strain response (Ai et al., 2016; Meng et al., 2021), and strength characteristics can change markedly (Zhang et al., 2015a; Kong et al., 2021). However, regarding the influence of temperature on the brittle–ductile transition, most experiments have indicated that temperatures above 400 °C are required to induce a pronounced effect, which is far higher than the reservoir temperatures in currently developed intervals (Gabova et al., 2020; Ranjith et al., 2012). Consequently, conventional understanding has tended to emphasize the pressure sensitivity of brittle–ductile transition mechanisms, while largely neglecting temperature effects (Zhang et al., 2016; French et al., 2022; Meng et al., 2021). In recent years, with improvements in ultra-deep coring technology and high pressure and high pressure (HPHT) laboratory facilities, it has become feasible to conduct rock mechanical tests on deep to ultra-deep cores under conditions close to in-situ HTHP environments (Cheng et al., 2023; Zhao et al., 2025b). Existing studies have shown that, with increasing burial depth, the fraction of brittle minerals in the reservoir generally increases, and rocks within typical deep burial depths (3500–4500 m) still exhibit predominantly brittle behavior (Xie et al., 2021). Meanwhile, under high confining pressure, the temperature threshold required to induce a brittle–ductile transition decreases significantly, and the corresponding pressure-temperature window overlaps with the actual geological conditions of deep to ultra-deep reservoirs (Jefferd et al., 2021; Liu et al., 2023a; Roy and Singh, 2023). Nevertheless, systematic rock mechanical tests on ultra-deep downhole cores under HTHP conditions are still very limited.

Creating a complex fracture network with high flow conductivity by hydraulic fracturing is one of the key approaches to efficiently developing deep to ultra-deep tight reservoirs (Zhang et al., 2025b; Lei et al., 2022; Liu et al., 2023b). In recent years, field experience has shown that some ultra-deep reservoirs exhibit low and rapidly decaying fracture conductivity and limited effectively stimulated reservoir volume after fracturing (Zhao et al., 2025a). To elucidate the initiation and propagation mechanisms of fractures in deep to ultra-deep reservoirs, numerous true triaxial hydraulic fracturing experiments have been conducted (Barbot and Zhang, 2023; Hou et al., 2017b; Zhu et al., 2023). However, most of these studies are still restricted to shallow to deep conditions (minimum horizontal effective principal stress <30 MPa, temperature <100 °C) and therefore cannot faithfully reproduce fracture evolution under in-situ HTHP conditions in deep to ultra-deep reservoirs (Yu et al., 2024). On the other hand, accurately predicting break-down pressure is a prerequisite for safe and efficient fracturing operations (Hou et al., 2017a; Zhu et al., 2025). Conventional break-down model (H-W model) and poro-elastic break-down model (H-F model) are widely used in engineering practice owing to their simple forms and convenient parameterization, but they usually ignore thermally induced stresses (Haimson and Fairhurst, 1969; Sampath et al., 2018; Wu et al., 2020). In ultra-deep reservoirs, formation temperature increases significantly with burial depth, and the temperature difference between fracturing fluid and formation rock can induce thermal stresses that modify rock mechanical properties and strongly affect fracture initiation and propagation, thereby introducing non-negligible prediction errors (Li et al., 2021; Zhuang et al., 2022; Kong et al., 2021). It is therefore necessary to systematically compare break-down models that incorporate temperature effects with conventional models, in order to clarify their applicability and limitations in deep to ultra-deep reservoirs.

In this context, the present study uses ultra-deep downhole cores to conduct triaxial compression tests under HPHT conditions. By analyzing failure modes, stress–strain responses, and energy-based brittleness indices, we comprehensively evaluate the main features of the brittle–ductile transition of ultra-deep rocks and its sensitivity to pressure and temperature. In addition, true triaxial hydraulic fracturing experiments are designed on 200 mm × 200 mm × 200 mm sandstone cubes. Injection pressure–time curves, three-dimensional fracture geometries reconstructed from computed tomography (CT) scans, and break-down pressures are jointly used to systematically investigate fracture initiation and propagation behavior under HPHT conditions. Furthermore, four classical break-down pressure models are introduced and their applicability to deep and ultra-deep reservoir conditions is comparatively assessed. The overall aim is to elucidate, in a systematic manner, the evolution of rock mechanical properties after the brittle–ductile transition and the mechanisms of fracture initiation and propagation in ultra-deep tight reservoirs, thereby providing experimental and theoretical support for optimizing hydraulic fracturing design and enhancing the development efficiency of ultra-deep reservoirs.

2. Materials and experimental methodology

2.1. Triaxial compression tests

2.1.1. Cylindrical rock samples

The western uplift of the Junggar Basin in China is rich in deep and ultra-deep oil and gas resources, among which ultra-deep tight reservoirs at depths greater than 5000 m are key targets for future large-scale reserve growth. In this study, full-diameter downhole cores from a representative well, Well X5, were selected as the research object, with the main coring interval ranging from 5470.3 to 5478.5 m. To ensure the reliability of the experimental results, core samples were preferentially taken from adjacent depth intervals and only those with intact

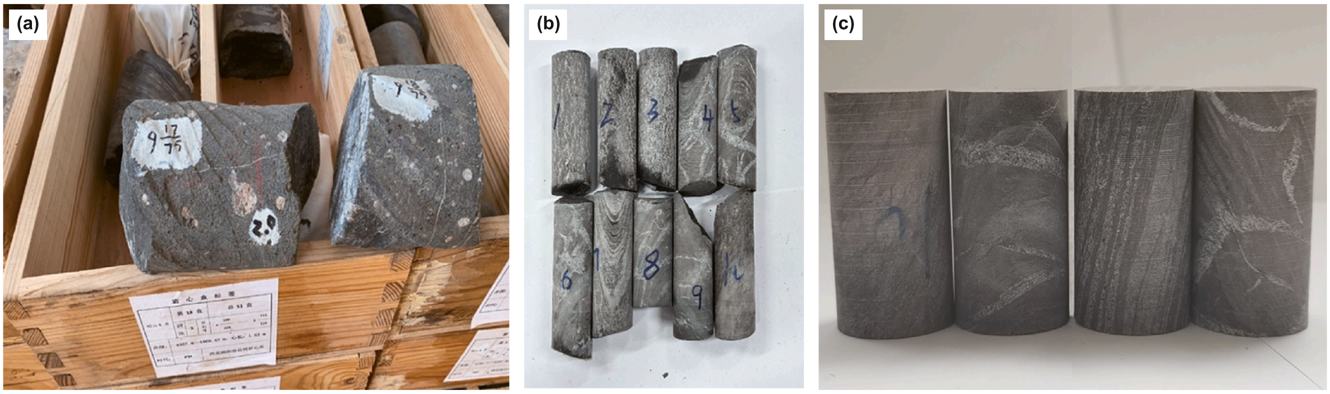

Fig. 1. Ultra-deep rock specimens. **(a)** Full-diameter downhole cores; **(b)** Cylindrical blanks; **(c)** Standard cylindrical specimens.

structure and suitable geometry for standard specimen preparation were used (Fig. 1(a)). X-ray diffraction analysis indicates that the minerals in this interval are mainly plagioclase (17.4%), quartz (14.6%), dolomite (43.6%), calcite (1.1%), and clay minerals (9.9%). This implies that the total content of brittle minerals is approximately 60%, whereas the content of weak minerals (clays) is less than 10% (Herrmann et al., 2018). As shown in Fig. 1(b), cylindrical blanks with a diameter of 25 mm and a length greater than 50 mm were first drilled from the full-diameter cores. Subsequently, following the specimen preparation procedures recommended by the International Society for Rock Mechanics (ISRM) (Ulusay and Hudson, 2007), the ends of the cylinders were cut and finely ground, and the end non-parallelism and surface flatness were controlled within 0.05 mm and 0.02 mm, respectively. In this way, standard cylindrical specimens with a diameter of 25 mm and a height of 50 mm were prepared for mechanical testing (Fig. 1(c)).

To systematically elucidate the evolution of rock mechanical properties under the combined effects of temperature and confining pressure in deep and ultra-deep reservoirs, simulated depths of 3500–5000 m are defined in this study as "deep reservoir conditions", whereas simulated depths greater than 5000 m are defined as "ultra-deep reservoir conditions". The formation pressure at the coring well is close to hydrostatic, and the regional in-situ stress and temperature conditions are characterized by maximum and minimum horizontal stress gradients of approximately 0.018–0.022 MPa/m and 0.0198–0.020 MPa/m, respectively, and a geothermal gradient of about 24.3 °C/km (Meng et al., 2022; Sun et al., 2023). Based on these geological constraints, ten triaxial compression test conditions were designed to represent different burial depths. Furthermore, the experimental design was divided into two categories: (1) high pressure and ambient temperature (HPAT) conditions and (2) HPHT conditions, in order to further investigate the temperature sensitivity of the mechanical behavior of ultra-deep core samples under high pressure. The combinations of confining pressure, temperature, and corresponding simulated burial depth for each condition are summarized in Table 1.

2.1.2. *Experimental equipment and testing procedure*

All triaxial compression tests were conducted using a GCTS RTR-1500 HPHT rock triaxial testing system, which consists of eight main functional modules, including servo loading and temperature control (Hou et al., 2017a). The RTR-1500 is a closed-loop digital servo-controlled system capable of strain-controlled or stress-controlled loading, post-failure mechanical behavior tests under triaxial conditions, while complying with the relevant rock mechanics testing standards of the ISRM. The main technical specifications of the system are: frame stiffness of 10000 kN/mm, dynamic loading frequency of 0–10 Hz, maximum axial load of 1500 kN (with an accuracy of 0.25%), maximum confining and pore pressure of 210 MPa, and a maximum operating temperature of 200 °C. Axial and radial deformations are recorded by linear variable differential transformers (LVDTs), with a measurement error less than 0.15% of full scale.

Prior to testing, the prepared standard cylindrical specimens were dried in an oven at 40 °C for 48 h to ensure a near-dry initial condition. During the tests, each specimen was wrapped with a heat-shrink sleeve to prevent oil infiltration, placed into the pressure vessel, and instrumented with axial and circumferential LVDTs. The main testing steps were as follows: (1) Apply a 2 MPa axial load to stabilize the specimen, and then increase the confining pressure to the target value; (2) Raise the temperature to the target value at a heating rate of 2 °C/min and hold for 1 h to ensure a uniform internal temperature; (3) Load axially at a rate of

Table 1
Experimental conditions for triaxial compression tests.

Experimental conditions	Specimen, #	Simulated depth, m	Confining pressure, MPa	Temperature, °C
HPAT	1	5000	100	20
	2	5500	110	20
	3	6000	120	20
	4	6500	130	20
	5	7000	140	20
HPHT	6	5000	100	120
	7	5500	110	130
	8	6000	120	140
	9	6500	130	150
	10	7000	140	160

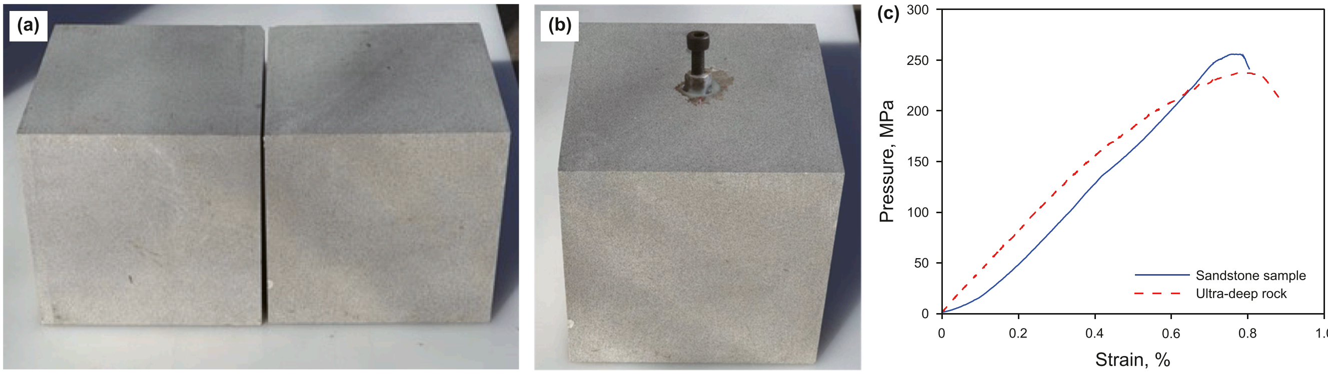

Fig. 2. True triaxial fracturing experiment specimens. **(a)** Cubic sandstone specimen; **(b)** Sealed steel pipe; **(c)** Comparison of triaxial compression results.

0.05 mm/min until specimen failure; (4) Continuously record the stress–strain curves throughout the test.

2.2. True triaxial hydraulic fracturing experiments

2.2.1. Cubic rock samples

To compare fracture initiation and propagation behavior under deep and ultra-deep reservoir conditions, true triaxial hydraulic fracturing experiments were conducted under simulated burial depths of 3500 and 5500 m. Due to the limited size of downhole cores, sandstone blocks with mechanical properties comparable to the ultra-deep core were used instead, with a Young's modulus $E = 36$ GPa, Poisson's ratio $\nu = 0.2$, and tensile strength $\sigma_t = 5$ MPa (Fig. 2(c)). The sandstone was machined into cubic specimens with dimensions of 200 mm × 200 mm × 200 mm, and a borehole with a diameter of 22 mm and a depth of 150 mm was drilled at the specimen center. A steel injection tube with an outer diameter of 16 mm, inner diameter of 6 mm, and length of 100 mm was then installed in the borehole. The annulus between the tube and the borehole wall was sealed and fixed using high temperature resistant epoxy, leaving a 70 mm open-hole section at the borehole end to serve as the hydraulic fracturing interval (Fig. 2(a) and (b)). The applied principal stresses and temperature conditions for each experiment case are summarized in Table 2.

2.2.2. Experimental equipment

The true triaxial hydraulic fracturing experiments were carried out using a multi-physics deep resource fracturing system (Chen et al., 2025b, 2025c). The system consists of an operation console, a true triaxial experimental apparatus, a servo-controlled triaxial loading system, a high-pressure fluid injection system, and flow and pressure monitoring modules (Fig. 3(a)). For cubic specimens with a side length of 200 mm, the system can provide a maximum confining stress of 160 MPa, a maximum injection pressure of 120 MPa, and a maximum injection rate of 66 mL/min. After testing, an industrial CT scanner (Phoenix V|tome|x S240) was used to characterize the fracture geometry. The scanner provides a spatial resolution as fine as 1 μm, with a maximum pixel resolution better than 2 μm (Fig. 3(b)).

2.2.3. Experimental procedure

Under high temperature conditions, the specimens were preheated to the target temperature at a rate of 10 °C/h and then held for 24 h to ensure that thermal equilibrium was reached. Under ambient temperature conditions, the specimens were oven-dried at 36 °C.

During testing, each specimen was placed in the true triaxial cell, and the three principal stresses were applied stepwise to their target values until a stable equilibrium state was achieved. Subsequently, fracturing fluid injection was initiated. The hydraulic fracturing process was considered complete when a sustained drop in injection pressure was observed. After fracturing, a core with a diameter of 100 mm and a length of 200 mm was drilled along the borehole axis from each cubic specimen and prepared for subsequent CT scanning (Fig. 3(c)).

3. Results

3.1. Analysis of the mechanical properties of ultra-deep rocks based on triaxial compression tests

3.1.1. Failure modes

In this section, the crack types and failure modes of the specimens after triaxial compression under different confining pressures and temperatures are compared to characterize the failure behavior of rocks under ultra-deep reservoir conditions.

As shown in Fig. 4(a), under HPAT conditions, the failure mode progressively evolves from brittle failure to ductile deformation with increasing confining pressure. At low confining pressure (100 MPa), the specimen develops combined tensile–shear cracks accompanied by local spalling of rock fragments, indicative of pronounced brittle instability. When the confining pressure increases to 100–130 MPa, the cracks transition to predominantly shear cracks, and a macro-shear failure plane forms inside the

Table 2
Experimental conditions for hydraulic fracturing experiments.

Experimental conditions	Specimen, #	Simulated depth, m	Fluid type	μ, mPa·s	Q_0, mL/min	T, °C	σ_v, MPa	σ_h, MPa	σ_H, MPa
Deep reservoir condition	1	3500	Slickwater	2.5	10	36	50	35	41
	2	3500	Slickwater	2.5	10	90	50	35	41
Ultra-deep reservoir condition	3	5500	Slickwater	2.5	10	36	75	53	62
	4	5500	Slickwater	2.5	10	130	75	53	62

Note: Q_0 represents flow rate, T represents temperature, σ_v represents vertical effective stress, σ_h represents minimum horizontal effective principal stress, and σ_H represents maximum horizontal effective principal stress.

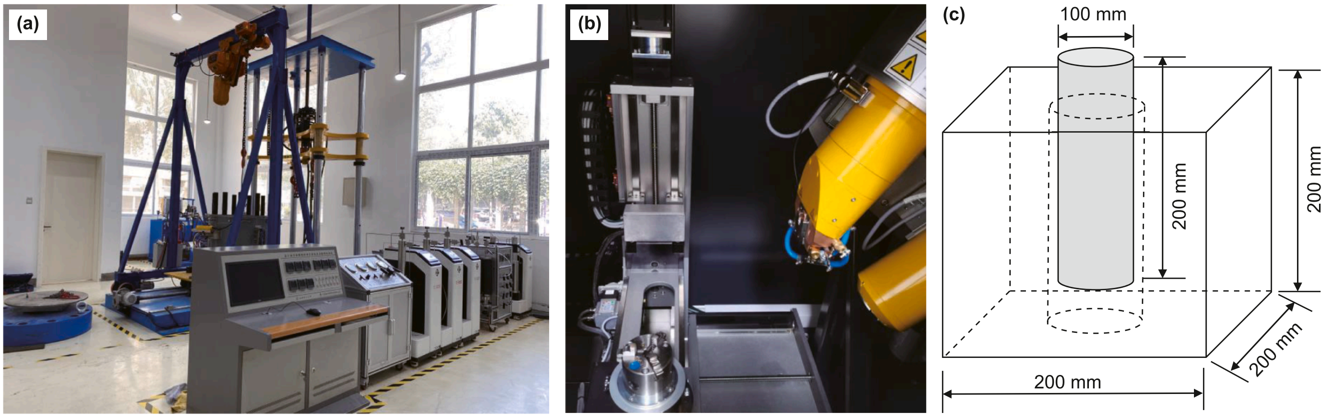

Fig. 3. Ture triaxial fracturing experimental equipment. (**a**) Multi-physics deep resource fracturing system; (**b**) Industrial CT scanner; (**c**) Schematic diagram of core sampling from cubic specimen.

specimen. Macroscopically, the rock fails along a preferentially oriented shear plane in a brittle characteristic. When the confining pressure is further increased to 140 MPa, multiple shear cracks are observed on the specimen surface but do not coalesce into a continuous failure plane, while pronounced bulging deformation develops in the central region. This indicates that the formation of a macro-shear failure plane is inhibited, microcrack propagation becomes more stable, and the overall failure mode shifts toward ductile deformation.

As shown in Fig. 4(b), under HPHT conditions, the combined increase in confining pressure and temperature promotes the evolution of the failure mode from brittle failure toward ductile deformation. At low confining pressure and temperature (100 MPa–120 °C), the specimen is dominated by shear cracks with a distinct macro-shear plane, and the failure mode is similar to that observed under HPAT conditions at 100–130 MPa, still reflecting a strongly brittle response. As confining pressure and temperature increase (i.e., 110 MPa–130 °C and 120 MPa–140 °C),

Fig. 4. Failure modes of ultra-deep rocks under different conditions. (**a**) HPAT conditions; (**b**) HPHT conditions.

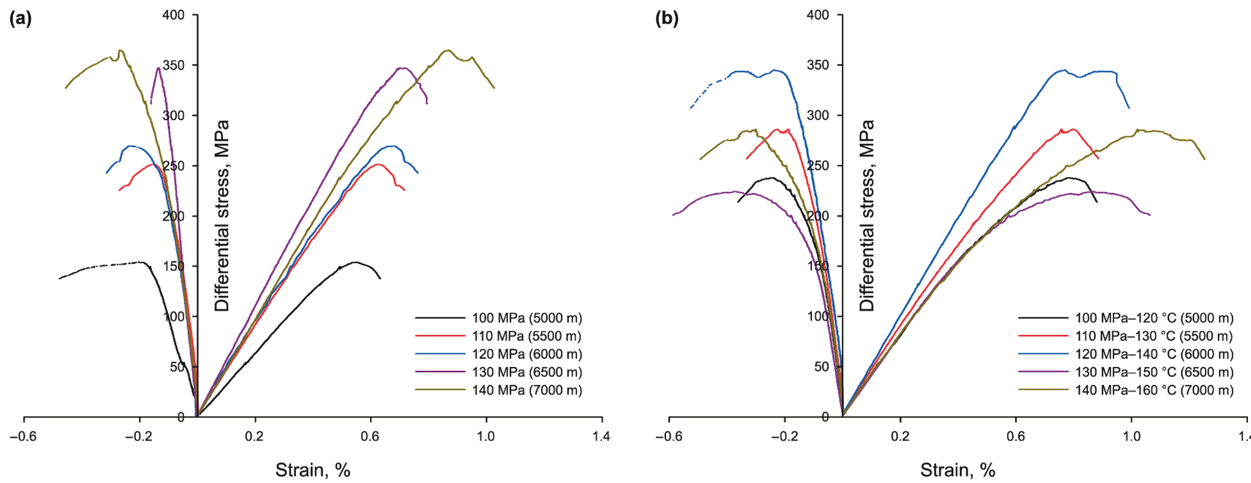

Fig. 5. Stress–strain curves of ultra-deep rocks under different conditions. **(a)** HPAT conditions; **(b)** HPHT conditions.

the cracks evolve into shear-dominated cracks or conjugate shear cracks, and macro-shear failure planes are still present, indicating that the rock remains in a brittle failure mode. When the confining pressure and temperature are further increased to 130 MPa–150 °C and 140 MPa–160 °C, a large number of fine microcracks develop on the specimen surface, pronounced bulging deformation occurs in the central region, and the overall failure mode becomes more consistent with a distributed cataclastic flow (Wu et al., 2000; Zhang et al., 2023). This demonstrates that, under the combined effect of high confining pressure and high temperature, the dominant failure mechanism gradually transitions from brittle failure to ductile deformation.

3.1.2. Deformation behaviors

In this section, the stress–strain responses and mechanical parameters of the specimens under different confining pressures and temperatures are compared to elucidate the deformation characteristics of rocks under ultra-deep reservoir conditions (Fig. 5).

As shown in Fig. 5(a), under HPAT conditions, the stress–strain behavior gradually evolves from typical brittle to ductile with increasing confining pressure. At relatively low confining pressures (100–130 MPa), the stress–strain curves have similar shapes: the pre-peak stage is essentially linear, whereas the post-peak stage exhibits a sharp stress drop, indicative of typical brittle failure. When the confining pressure is increased to 140 MPa, the stress–strain curve shows a clear brittle–ductile transition: the stress first increases linearly in the pre-peak stage, then the rate of stress increase decreases as it approaches the peak stress, and in the post-peak stage a short stress plateau appears before the curve occurs the strain softening.

As summarized in Table 3, changes in confining pressure substantially modify the mechanical properties of the ultra-deep rock. As the confining pressure increases from 100 to 140 MPa, the lateral confinement is progressively enhanced and the peak stress, peak strain, and Young's modulus all increase. Specifically, the peak stress, peak strain, and Young's modulus increase by 137%, 41.8%, and 43.3%, respectively, demonstrating strong pressure sensitivity. It is noteworthy that when the confining pressure rises from 100 to 110 MPa, the crack types change from combined tensile–shear cracks to predominantly single shear cracks, accompanied by a marked increase in both peak stress and peak strain. This indicates that the transition in crack type is accompanied by marked changes in both load bearing capacity and deformability.

As shown in Fig. 5(b), under HPHT conditions, the combined increase in confining pressure and temperature promotes the evolution of mechanical behavior from brittle to ductile. At relatively low confining pressures and temperatures (100 MPa–120 °C and 110 MPa–130 °C), the stress–strain curves are still dominated by brittle characteristics: the pre-peak response is nearly linear and the post-peak stage exhibits distinct strain softening. When the confining pressure and temperature are raised to 120 MPa–140 °C, an obvious stress plateau develops in the post-peak stage, reflecting a brittle–ductile transitional behavior. With a further increase in confining pressure and temperature to 130 MPa–150 °C and 140 MPa–160 °C, ductile features become more pronounced: the amount of plastic strain in the pre-peak stage increases significantly, and after the peak stress, the curves quickly enter a long stress plateau, during which the overall stress level tends to stabilize.

Table 4 shows that confining pressure and temperature jointly exert a strong control on the mechanical properties of ultra-deep rocks. As the loading condition increases from 100 MPa–120 °C to 120 MPa–140 °C, the peak stress and Young's modulus increase by 45% and 30%, respectively. When the condition is further increased to 140 MPa–160 °C, the peak stress and Young's modulus decrease by 17% and 21%, respectively, relative to those at

Table 3
Experimental results of triaxial compression tests under HPAT conditions.

Specimen, #	Simulated depth, m	Peak stress, MPa	Peak strain, %	Young's modulus, GPa	Poisson's ratio
1	5000	153.87	0.55	32.8	0.26
2	5500	251.17	0.63	44.5	0.14
3	6000	269.44	0.68	44.5	0.19
4	6500	346.26	0.69	54.6	0.21
5	7000	364.65	0.78	47.0	0.21

Table 4
Experimental results of triaxial compression tests under HPHT conditions.

Specimen, #	Simulated depth, m	Peak stress, MPa	Peak strain, %	Young's modulus, GPa	Poisson's ratio
6	5000	237.91	0.78	38.0	0.18
7	5500	286.21	0.76	41.9	0.17
8	6000	344.95	0.77	49.5	0.18
9	6500	224.18	0.86	39.0	0.22
10	7000	284.84	1.04	39.0	0.18

120 MPa–140 °C, whereas the peak strain increases by 35%. In conjunction with Fig. 4, this suggests that the reductions in peak stress and Young's modulus are mainly associated with a shift in failure mode from localized brittle shear failure to distributed cataclastic flow, during which microcracks become more abundant and fracture toughness is reduced. Similar trends were reported by Jefferd et al. (2021) for sandstone in triaxial compression tests under HPHT conditions, and were likewise attributed to the nucleation and stable growth of numerous microcracks leading to macroscopic strength degradation.

A comparison between HPAT and HPHT conditions shows that at relatively low confining pressures (100–120 MPa), the peak stress, peak strain, and Young's modulus are all higher at elevated temperature than at ambient temperature. For example, at a confining pressure of 100 MPa, the peak stress, peak strain, and Young's modulus under high-temperature conditions are 55%, 42%, and 16% higher, respectively, than those under ambient temperature conditions. This behavior can be explained by the fact that, in a high confining pressure environment, elevated temperature promotes thermal expansion of mineral grains and closure of pre-existing microcracks, thereby strengthening grain contacts and enhancing the load bearing capacity. In contrast, at higher confining pressures (130–140 MPa), the peak stress and Young's modulus become lower at high temperature than at ambient temperature, while the peak strain increases significantly. At 140 MPa, the peak stress and Young's modulus under high temperature conditions are 22% and 17% lower, respectively, than those under ambient temperature conditions, whereas the peak strain is 33% higher. This indicates that elevated temperature strongly promotes the brittle–ductile transition of ultra-deep rocks and markedly enhances their ductile deformation capacity. Overall, these results demonstrate that the brittle–ductile transition of rocks under ultra-deep conditions is temperature sensitive, and that the associated changes in failure mode, stress-strain response, and mechanical properties arise from the competition among multiple mechanisms (Ranjith et al., 2012; Kong et al., 2021).

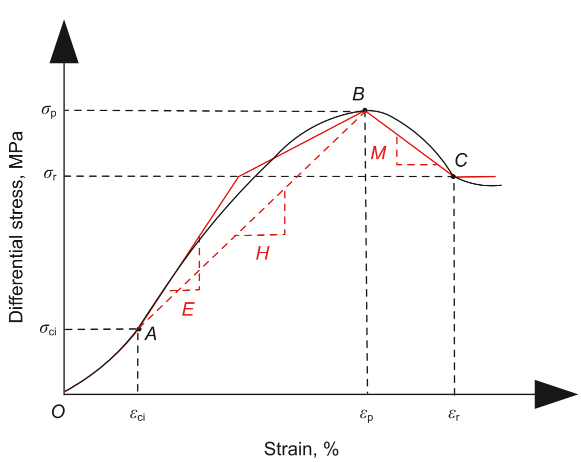

Fig. 6. Typical stress–strain curve of rock in triaxial compression test.

3.1.3. Brittle–ductile characteristics

In this section, the brittleness of the specimens under different confining pressures and temperatures is quantitatively evaluated, in order to clarify the brittle–ductile characteristic of rocks under ultra-deep reservoir conditions. During loading and failure, the rock continuously accumulates, dissipates, and transforms energy, and these processes can be effectively reflected by the stress–strain curves. Fig. 6 illustrates the key parameters on the stress–strain curve used to calculate the brittleness indices (Xie et al., 2021). Point A represents the stress level at which the intrinsic microcracks within the rock are fully closed, determined following the method proposed by Wen et al. (2023). Point B denotes the peak stress and point C corresponds to the stress level immediately before entering the residual stress stage. H and M represent the hardening modulus and the unloading modulus, respectively.

An energy-based brittleness index is adopted in this study to quantitatively characterize the brittle–ductile characteristic of the rocks (Eq. (1)), explicitly accounting for both the pre-peak and post-peak stages. The pre-peak brittleness index (B_{pre}) is defined as the ratio of the dissipated energy to the accumulated elastic energy before peak stress, whereas the post-peak brittleness index (B_{post}) is defined as the ratio of the fracture energy to the released elastic energy after peak stress (Tarasov and Potvin, 2013; Zhu et al., 2025). On this basis, a composite brittleness index (B_k) is constructed by combining B_{pre} and B_{post} with equal weights ($\alpha = \beta = 0.5$), to describe the overall brittle–ductile characteristics of the rock (Zhao et al., 2025b). When $B_k < 1$, the global response is dominated by brittle characteristic, whereas $B_k > 1$ indicates progressively more ductile characteristic. It should be emphasized that larger values of B_{pre}, B_{post}, and B_k correspond to more pronounced ductile characteristics (Tarasov and Potvin, 2013; Xie et al., 2021).

$$\begin{aligned} B_k &= \alpha B_{pre} + \beta B_{post} = \alpha \frac{E-H}{H} + \beta \frac{M-E}{M} \\ &= \alpha\left(\frac{\Delta\sigma_L}{\Delta\varepsilon_L} - \frac{\sigma_p - \sigma_{ci}}{\varepsilon_p - \varepsilon_{ci}}\right) \Big/ \left(\frac{\sigma_p - \sigma_{ci}}{\varepsilon_p - \varepsilon_{ci}}\right) + \beta\left(\frac{\sigma_r - \sigma_p}{\varepsilon_r - \varepsilon_p} - \frac{\Delta\sigma_L}{\Delta\varepsilon_L}\right) \Big/ \left(\frac{\sigma_r - \sigma_p}{\varepsilon_r - \varepsilon_p}\right) \end{aligned} \tag{1}$$

where $\Delta\sigma_L$ is the stress difference between two points on the linear portion of the stress–strain curve, MPa; $\Delta\varepsilon_L$ is the corresponding axial strain difference, %; σ_p is the peak stress, MPa; σ_{ci} is crack initiation stress, MPa; σ_r is the residual stress, MPa; ε_{ci} the crack initiation strain, %.

The B_{pre}, B_{post}, and B_k obtained under different conditions are presented in Fig. 7. As shown in Fig. 7, under HPAT conditions, the overall ductility first decreases and then increases with increasing confining pressure. When the confining pressure increases from 100 to 120 MPa, B_k decreases from 1.43 to 1.24, decreasing by 13.3%, indicating that, within this relatively low confining pressure

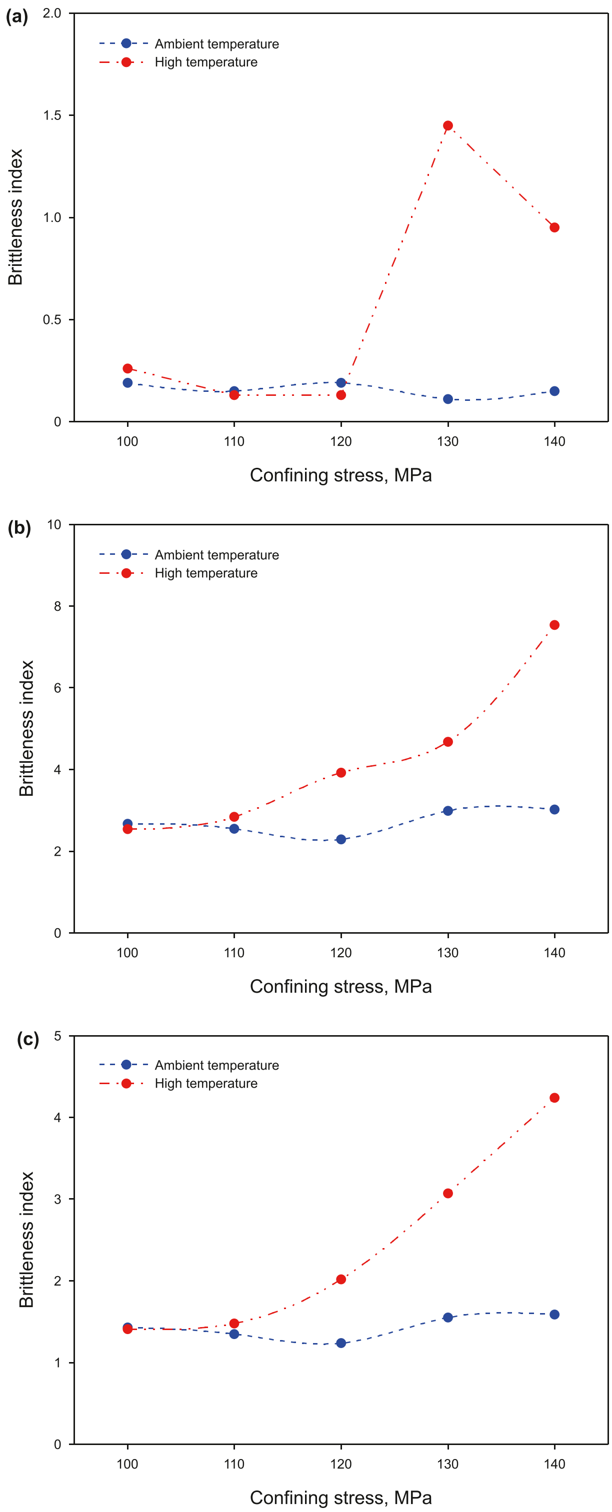

Fig. 7. Brittleness indies of ultra-deep rocks under different conditions. **(a)** B_{pre}; **(b)** B_{post}; **(c)** B_k.

range, the strengthening of lateral confinement makes the rock behave more brittle. When the confining pressure is further increased from 120 to 140 MPa, B_k increases from 1.24 to 1.59, increasing by 28.2%. This suggesting that, at higher confining pressures, further pore compaction and the more stable growth of numerous microcracks during triaxial compression lead to a gradual enhancement of rock ductility. It is noteworthy that as the confining pressure increases from 100 to 140 MPa, B_{pre} changes only slightly, from 0.19 to 0.15. This small variation implies that, under HPAT conditions, the confining pressure dependence of the overall ductility is mainly governed by the post-peak stage, and that the enhancement of post-peak ductility plays a dominant role in increasing the overall ductile characteristic.

Under HPHT conditions, the rock ductility increases markedly with increasing confining pressure and temperature. When experimental conditions increase from 100 MPa–120 °C to 140 MPa–160 °C, B_k rises from 1.41 to 4.24, corresponding to an increase of 200.7%. This clearly demonstrates that the combined effect of high confining pressure and high temperature strongly promotes the transition from brittle to ductile characteristic. Unlike the HPAT condition, although B_{pre} exhibits only minor changes between 100 MPa–120 °C and 120 MPa–140 °C, it sharply increases from 0.13 to 0.95 (an increase of 630.8%) when the conditions are further elevated to 140 MPa–160 °C. In this condition, the proportion of dissipated energy before peak stress increases substantially, indicating that pre-peak plastic deformation and energy dissipation are significantly enhanced and that pre-peak ductile deformation becomes an important contributor to the overall ductile characteristic.

A comparison between HPAT and HPHT conditions shows that, at relatively low confining pressures (100–110 MPa), the three indices B_{pre}, B_{post}, and B_k are similar for the two temperature conditions, implying that within this stress range the high temperature environment corresponding to the simulated depth has only a limited influence on the brittle–ductile characteristics. However, as the confining pressure is further increased to 120–140 MPa, both B_{pre} and B_{post} under high temperature conditions become significantly larger than those under ambient temperature conditions, and the overall ductility is markedly enhanced. For example, at 140 MPa, B_k increases from 1.59 (under HPAT) to 4.24 (under HPHT), increasing by 166.7%. Together with Figs. 4 and 5, this indicates that the temperature sensitivity of the brittle–ductile transition behavior of ultra-deep rocks is weak at relatively low confining pressures, whereas when the confining pressure approaches the critical range for the brittle–ductile transition, temperature effects are greatly amplified and can significantly accelerate the evolution from brittle to ductile characteristic (details see Section. 4.1).

3.2. *Analysis of fracture initiation and propagation characteristics based on true triaxial hydraulic fracturing experiments*

3.2.1. *Injection pressure response*

In this section, true triaxial hydraulic fracturing experiments were conducted on sandstone cubic specimens under different stress state and temperature conditions. The injection pressure–time curves were recorded in real time to elucidate the evolution of injection pressure associated with fracture initiation and propagation during continuous fluid injection (Fig. 8), where P_b denotes the break-down pressure, P_p denotes the propagation pressure.

Fig. 8(a) and (b) show the injection pressure-time curves under deep reservoir conditions (simulated depth of 3500 m), which can be divided into four stages corresponding to different behaviors of the hydraulic fracturing process. Taking the ambient temperature condition as an example, in Stage I the injected fluid mainly fills the pipeline and open-hole section of the borehole, and the pressure variation is limited. In Stage II, fluid continuously accumulates around the borehole and enhances stress concentration in the near-wellbore region, leading to an approximately linear increase in injection pressure. When the circumferential stress at the

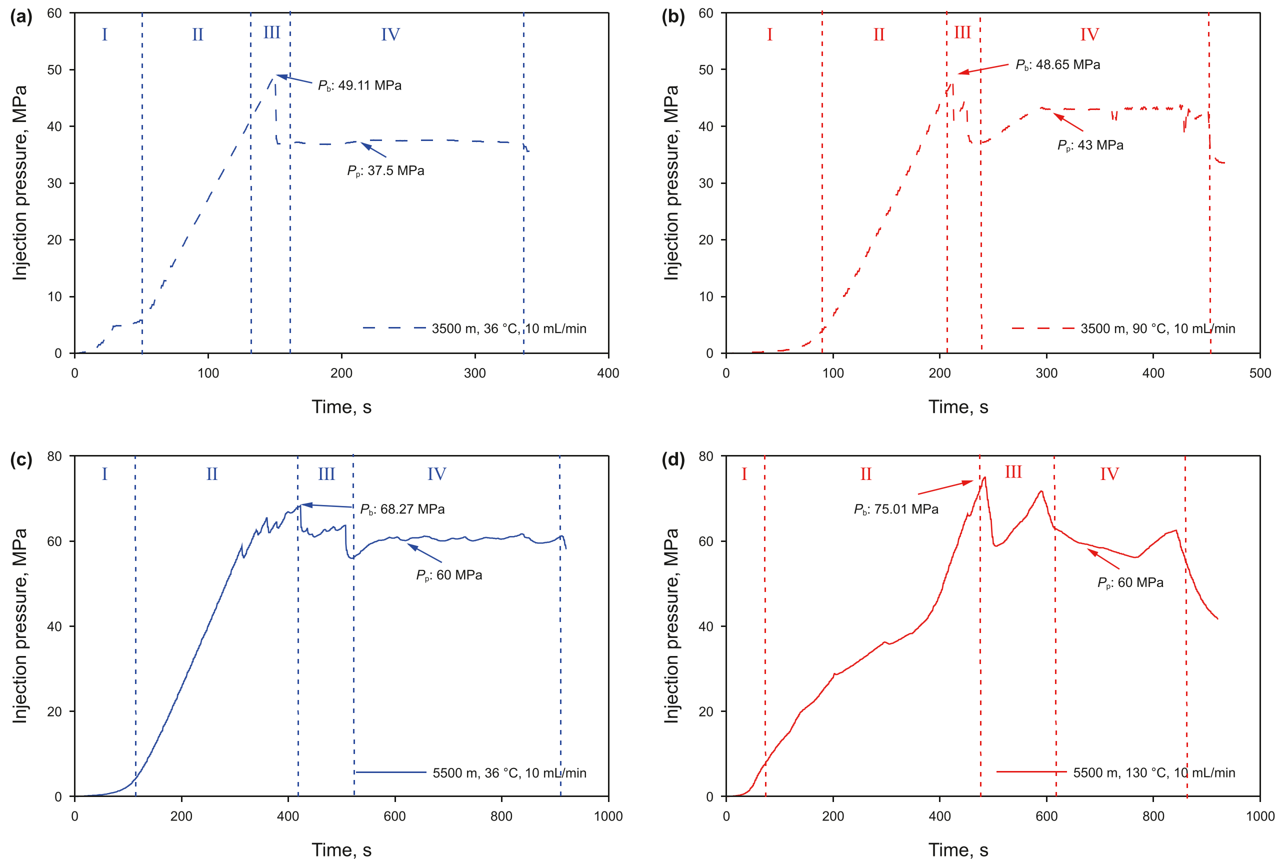

Fig. 8. The injection pressure–time curves under different conditions. **(a)** Deep reservoir condition at ambient temperature; **(b)** Deep reservoir condition at high temperature; **(c)** Ultra-deep reservoir condition at ambient temperature; **(d)** Ultra-deep reservoir condition at high temperature.

borehole wall increases to the tensile strength of the rock, Stage III begins: fracture initiation occurs and the injection pressure reaches its peak. The rapid formation of the fracture creates a new flow pathway, causing a sharp pressure drop. In Stage IV, the fracture continues to propagate along the maximum horizontal principal stress direction. Further growth must overcome both the minimum horizontal principal stress and the rock tensile strength, and the injection pressure gradually approaches a quasi-steady level. It is noteworthy that under high temperature conditions (90 °C), the injection pressure–time curve in Stage III exhibits a pronounced double-peak feature, indicating that the propagating fracture temporarily arrests and is subsequently reactivated. The second pressure peak is almost equal to the stable propagation pressure, which mainly results from a mismatch between the fluid injection rate and the fracture propagation rate.

Fig. 8(c) and (d) present the injection pressure-time curves under ultra-deep reservoir conditions (simulated depth of 5500 m). Similar to the deep reservoir condition, the curves can still be divided into four stages, but their evolution is more complex, and the response characteristics and physical implications in some stages differ. Under ambient temperature condition, the injection pressure in Stage II initially increases approximately linearly, but the pressurization rate decreases as breakdown is approached. Compared with the deep reservoir condition, in Stages III and IV the pressure drops sharply after reaching the breakdown pressure, and the post-peak pressure exhibits stronger oscillations, implying that the fracture experiences greater resistance during propagation. Under high temperature condition (130 °C), Stage II can be further divided into an initial nonlinear loading phase followed by a linear loading phase, with a noticeably higher pressurization rate in the linear phase. This behavior is mainly attributed to enhanced rock ductility and intensified local deformation around the borehole, which result in a more prolonged pore compaction process during the early pressurization stage (Cheng et al., 2023). It is also noteworthy that in Stages III and IV the pressure–time curve displays three distinct pressure peaks. The second peak is close to the breakdown pressure and significantly higher than the stable propagation pressure, indicating that the fracture may undergo multiple episodes of arrest and reactivation during propagation, requiring repeated rebuilding of injection pressure to sustain successive fracture propagation. Therefore, in ultra-deep reservoir environments, continuous and stable fracture propagation becomes more difficult to achieve, and the hydraulic fracturing process is characterized by stronger intermittency and complexity.

3.2.2. *Fracture morphology interpreted from CT scanning*

In this section, CT scanning is used to characterize in detail the fracture morphology generated inside the sandstone cubes after true triaxial hydraulic fracturing under different stress state and temperature conditions. First, the CT images are pre-processed based on grayscale information, and the fracture network is reconstructed in three dimensions following the method proposed by He et al. (2021). Then, the fractal dimension is introduced to quantitatively describe the geometric complexity of the hydraulic fractures under different conditions. A larger fractal dimension indicates a more complex fracture geometry.

Fig. 9(a) and (b) show the fracture morphology under deep reservoir conditions (simulated burial depth of 3500 m). At ambient temperature, the fracture surface is highly continuous

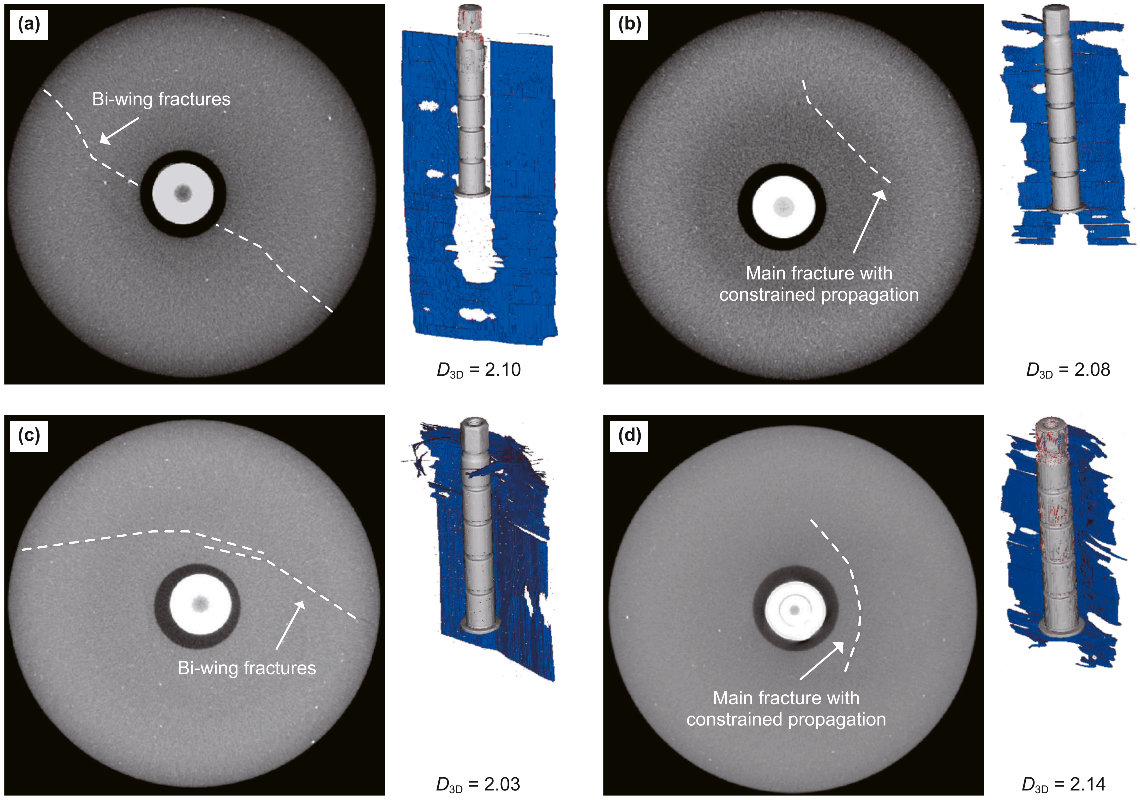

Fig. 9. The fracture morphology and fractal dimensions under different conditions. **(a)** Deep reservoir condition at ambient temperature; **(b)** Deep reservoir condition at high temperature; **(c)** Ultra-deep reservoir condition at ambient temperature; **(d)** Ultra-deep reservoir condition at high temperature.

and nearly propagates to the specimen boundaries, forming a symmetric bi-wing fracture geometry. At elevated temperature (90 °C), the fracture still propagates along the maximum horizontal principal stress direction, but the propagation distance is shorter and local regions exhibit a jagged configuration. The similar fractal dimensions at the two temperatures indicate that, under deep reservoir conditions, temperature has a limited influence on fracture complexity, although the spatial extent of the fracture is slightly larger at ambient temperature.

Fig. 9(c) and (d) show the fracture morphology under ultra-deep reservoir conditions (simulated burial depth of 5500 m). At ambient temperature, the fracture overall still maintains a bi-wing geometry. However, compared with the deep reservoir condition, the fractal dimension decreases from 2.10 to 2.03, suggesting that the higher stress level and larger horizontal stress difference constrain fracture propagation and reduce the geometric complexity of hydraulic fractures. At elevated temperature (130 °C), the enhanced rock ductility further restricts fracture propagation, and the fractures are mainly confined to the vicinity of the injection region. Nevertheless, compared with the deep reservoir condition at high temperature, the fractal dimension increases from 2.08 to 2.14, increasing by 2.9%. This indicates that under higher stress state and temperature, large-scale macro-fractures are suppressed, and fractures may undergo multiple cycles of initiation, arrest, and reactivation during propagation, leading to a more complex hydraulic fracture network.

3.2.3. Breakdown pressure

In this section, four classical break-down models are employed to analyze and compare the break-down pressures obtained from the true triaxial hydraulic fracturing experiments, with the aim of assessing their applicability under deep and ultra-deep reservoir conditions. All four models are based on a tensile strength criterion, under which fracture initiation is assumed to occur when the circumferential effective stress at the wellbore reaches the tensile strength of the rock. The circumferential effective stress at the borehole wall is expressed as the superposition of four stress components: the in-situ horizontal principal stresses, the wellbore internal pressure due to fluid injection, the stress field induced by fluid leak-off into the formation, and the thermal stress induced by the temperature variation at the wellbore (Fig. 10). These models are compact in form, have clear physical meaning for each parameter, and are convenient for field application. Furthermore, they also form the basis for many subsequent model extensions. Therefore, a systematic comparison of those four models are carried out in this study to clarify the sensitivity of break-down pressure to stress state and temperature in ultra-deep reservoirs and to provide guidance for further model refinement.

Hubbert and Willis (1957) proposed the conventional break-down model (H-W model) under the assumptions of a linear-elastic, intact and impermeable formation, with fracture initiation occurring at a point on the wellbore wall. Because the model neglects fluid leak-off and the additional stress field generated by pore pressure distribution in the surrounding rock, it tends to overestimate breakdown pressure (Sampath et al., 2018). By superimposing the thermal stress field derived by Deng et al. (2009) based on generalized Hooke's law and thermoelastic theory, onto the H-W model, a temperature-dependent conventional break-down model (the T-H-W model) can be obtained (Li et al., 2005; Stephens and Voight, 1982). The derivation of the thermal stress field is based on the following main assumptions: (1) axial heat conduction in the fluid is negligible compared with axial convection; (2) the thermal properties of the fluid (heat capacity, density, thermal conductivity, etc.) are weakly dependent on

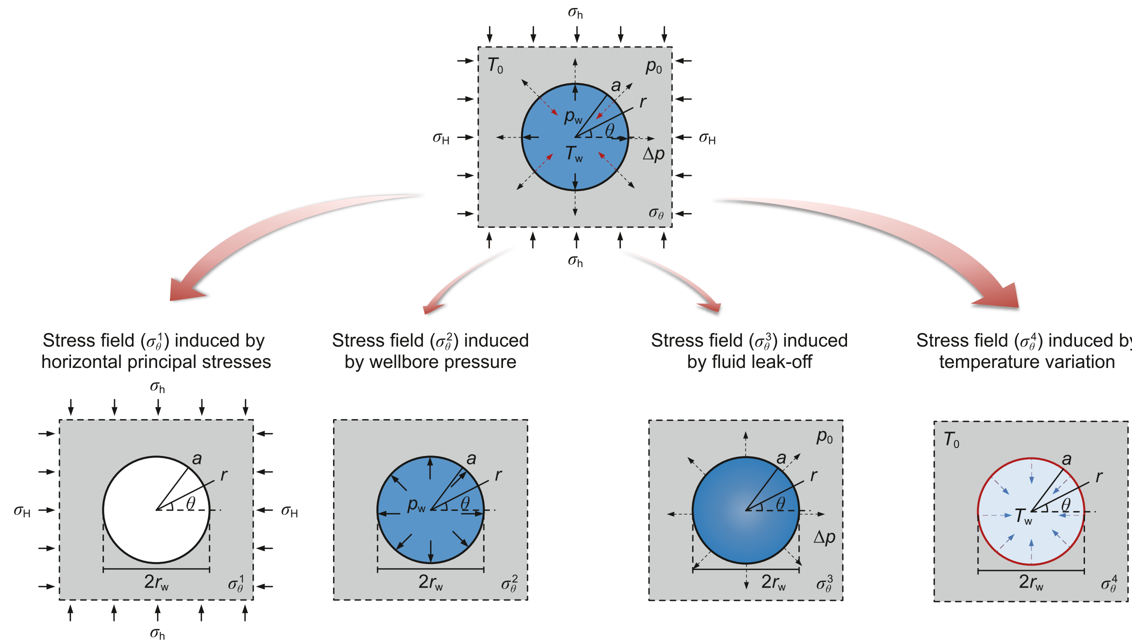

Fig. 10. Schematic diagram of the superposition of independent stress fields during hydraulic fracturing (Haimson and Fairhurst, 1969; Zhu et al., 2015; Wu et al., 2020).

temperature; and (3) the borehole is a smooth cylinder and the surrounding rock is an isotropic, linear-elastic medium that exchanges heat with the fluid only by conduction, with the borehole wall temperature held constant (Deng et al., 2009; Ju et al., 2025). A key limitation is that the resulting tangential thermal stress at the borehole wall is time-invariant, and the contribution of thermal stresses in regions away from the borehole wall is not considered. The corresponding expressions of the H-W and T-H-W models can be written as:

$$\begin{cases} p_\mathrm{b} = 3\sigma_\mathrm{h} - \sigma_\mathrm{H} - p_0 + \sigma_\mathrm{t} \ \ \text{(H-W model)} \\ p_\mathrm{b} = 3\sigma_\mathrm{h} - \sigma_\mathrm{H} - p_0 + \sigma_\mathrm{t} - \dfrac{E\alpha_\mathrm{m}}{3(1-\nu)}(T_0 - T_\mathrm{w}) \ \text{(T-H-W model)} \end{cases} \tag{2}$$

where p_0 is the formation pore pressure, MPa; α_m is the rock thermal expansion coefficient, °C^{-1}; T_0 is the initial formation temperature, °C; T_w is the temperature of fracturing fluid, °C.

Haimson and Fairhurst (1969) incorporated poro-elasticity into the elastic solution and proposed a poro-elastic break-down model (H-F model) for permeable formations. The main assumptions of this model are: (1) the rock is permeable; (2) the borehole cross-section is smooth and circular; (3) the formation has uniform permeability; and (4) the flow is axisymmetric and obeys Darcy's law (Wu et al., 2020). By explicitly considering the additional effective stress induced by fluid leak-off into the formation, the H-F model can better capture the influence of pore pressure distribution on break-down pressure. However, fracture initiation is still assumed to occur at the wellbore wall, and the spatial distribution of pore pressure in the rock mass around the wellbore is not fully described. Meanwhile, the model neglects the non-uniform pressure field in the near-wellbore region, which can lead to underestimation of break-down pressure under certain conditions. Superimposing the thermal stress field onto the H-F model yields a temperature-dependent poro-elastic break-down model (T-H-F model).

$$\begin{cases} p_\mathrm{b} = p_\mathrm{w} = \dfrac{3\sigma_\mathrm{h} - \sigma_\mathrm{H} + \sigma_\mathrm{t}}{2 - \alpha\dfrac{1-2\upsilon}{1-\upsilon}} + p_0 \ \text{(H-F model)} \\ p_\mathrm{b} = p_\mathrm{w} = \dfrac{3\sigma_\mathrm{h} - \sigma_\mathrm{H} + \sigma_\mathrm{t}}{2 - \alpha\dfrac{1-2\upsilon}{1-\upsilon}} + p_0 - \dfrac{E\alpha_\mathrm{m}}{3(1-\nu)}(T_0 - T_\mathrm{w}) \\ \qquad \text{(T-H-F model)} \end{cases} \tag{3}$$

where α is Biot's coefficient.

In this study, the mechanical parameters used in the four models are constrained by laboratory tests and existing data from the same block. Specifically, E, ν, and σ_t are taken from the mechanical tests on the sandstone specimens. The value of α is obtained from poro-elastic tests on sandstone cores with similar lithology in the same block (Kong et al., 2021). The T_0 and stress state are taken from geological data near the coring well. Previous studies have shown that, for sandstone, the α_m in the range 100–300 °C is typically on the order of 1×10^{-5}–3×10^{-5} °C^{-1} (Gong et al., 2025). In this work, a representative value of 2×10^{-5} °C^{-1} is used in the baseline calculations, and its influence is further examined in the parametric sensitivity analysis.

Since the parameter sensitivity of the H-W and H-F models has already been systematically investigated in previous studies, the present work focuses on the sensitivity of the T-H-W and T-H-F models to key thermo-mechanical parameters, namely E, the α_m, and the T_0 (Table 5) (Sampath et al., 2018; Wu et al., 2020). The corresponding numerical results are shown in Fig. 11.

Overall, compared with the H-W and H-F models, both T-H-W and T-H-F yield systematically lower break-down pressures, indicating that the additional thermal stress induced by wellbore cooling significantly reduces the circumferential effective stress at the wellbore wall and thus lowers the fracture initiation threshold. For fixed T_0 and α_m, the predicted break-down pressures of both temperature-dependent models decrease monotonically as E increases from 35 to 55 GPa, with reductions of 21% and 34.4% for the

Table 5
Basic parameters of the sensitivity analysis for the T-H-W model and T-H-F model.

Parameters	Values	Parameters	Values	Parameters	Values
E, GPa	35, 40, 45, 50, 55	σ_t, MPa	5	α_m, $\times 10^{-5}$ °C^{-1}	1, 1.5, 2, 2.5, 3
ν	0.2	σ_h, MPa	53	T_0, °C	120, 130, 140, 150, 160
α	0.8	σ_H, MPa	62	T_w, °C	36

T-H-W and T-H-F models, respectively. This suggests that, in stiffer rocks, the same temperature contrast generates larger thermal stresses, making fracture initiation easier. For fixed T_0 and E, increasing α_m from 1×10^{-5} to 3×10^{-5} °C^{-1} similarly leads to a monotonic reduction in the break-down pressure predicted by both models, with reductions of 31% and 46.4% for the T-H-W and T-H-F models, respectively. This reflects the promoting effect of thermally induced microcracking arising from thermal expansion mismatch among different mineral compositions. Previous work has shown that, within 100–300 °C, the α_m of sandstone increases only slowly and approximately linearly from about 1.4×10^{-5} to 2.6×10^{-5} °C^{-1}. Therefore, using a representative, nearly constant value of α_m for ultra-deep reservoir temperatures is reasonable for engineering prediction. For fixed α_m and E, increasing T_0 from 120 to 160 °C also causes the break-down pressure predicted by both models to decrease monotonically, which implies that higher formation temperatures amplify the temperature difference and thus impose stronger thermal shocks and thermal damage on the surrounding rock. This thermal effect becomes increasingly important at higher in-situ temperatures.

Fig. 12 compares the break-down pressures obtained from the true triaxial hydraulic fracturing experiments with the predictions of the four models. Under ambient temperature conditions, the T-H-W and T-H-F models degenerate to the H-W and H-F models, respectively, and their predictions coincide. Under deep reservoir conditions, the measured break-down pressures at the two temperatures are almost identical, indicating that break-down pressure is weakly sensitive to temperature at the simulated burial depth. Under ultra-deep reservoir conditions, however, the break-down pressure increases from 68.27 to 75.01 MPa when the temperature is raised from ambient to high temperature (130 °C), corresponding to an increase of 9.9%, which indicates that the break-down pressure becomes considerably more temperature-sensitive at the simulated burial depths.

To further evaluate the performance of each model under HPHT conditions, Table 6 summarizes the true triaxial hydraulic fracturing experiment results and field fracturing break-down pressures. Based on the stress state and temperature conditions used in the laboratory tests, the additional cases are roughly classified into deep and ultra-deep reservoir conditions, and the relative deviations between model predictions and measured break-down pressures are listed in Tables 7 and 8.

As shown in Table 7, under deep reservoir conditions, the H-F model yields the smallest prediction errors, generally within 18%, whereas the deviations of the H-W and T-H-F models are relatively larger. This indicates that, at lower stress state and temperature, the stress induced by fluid leak-off into the formation dominates the fracture initiation process, while the thermal stress induced by the limited temperature difference remains small. Compared with the T-H-W model, the H-F model reproduces the measured break-down pressures more closely under deep reservoir conditions, suggesting that H-F has better applicability and predictive reliability in this condition.

As shown in Table 8, under ultra-deep reservoir conditions, both the H-F and T-H-W models achieve prediction errors within 18%. Notably, the predictive performance of the H-W model improves under ultra-deep reservoir conditions: its maximum error decreases from 96.8% (deep reservoir) to 47.4% (ultra-deep reservoir), implying that, as confining stress increases, pore compaction reduces the impact of leak-off on the fracture initiation process. In contrast, the contribution of thermally induced stress becomes increasingly important at higher temperatures. Compared with deep reservoir conditions, the maximum error of the T-H-W model decreases from 26.3% to 17.3% in the ultra-deep reservoir condition, further highlighting the crucial role of thermal stress in ultra-deep reservoirs. Therefore, under ultra-deep reservoir conditions, the T-H-W model exhibits superior physical consistency and prediction reliability, and is more suitable for engineering applications.

4. Discussion

4.1. Mechanical property evolution of ultra-deep rocks

In ultra-deep reservoirs, the mechanical properties of rocks under HPHT have a direct impact on hydraulic fracturing performance and hydrocarbon recovery. In this study, triaxial compression tests on ultra-deep core samples were conducted under various confining pressures and temperatures. The evolution of the brittle–ductile transition under ultra-deep reservoir conditions was systematically investigated in terms of failure, deformation and brittle–ductile characteristics.

Under HPAT conditions, within the confining pressure range of 100–130 MPa (simulated depths of 5000–6500 m), the brittle–ductile transition of the ultra-deep rock shows only weak sensitivity to confining pressure. When the confining pressure is increased to 140 MPa, typical brittle–ductile transition features emerge: (1) the failure mode evolves from predominantly brittle failure with macro-shear failure plane to bulging deformation with multiple shear cracks; (2) a pronounced post-peak stress plateau appears in the stress–strain curve; and (3) the post-peak brittleness index increases, indicating enhanced ductile behaviour in the post-peak stage. By contrast, the pre-peak brittleness index remains nearly unchanged compared with that at lower confining pressures, suggesting that the pre-peak response is still dominated by brittle regime.

Under HPHT conditions, the rock exhibits overall strongly brittle characteristic within 100 MPa–120 °C to 110 MPa–130 °C (simulated depths of 5000–5500 m). At the same confining pressure, the stress–strain responses and brittleness indices at high temperature are similar to those at ambient temperature, suggesting that the influence of temperature on the brittle–ductile transition is limited in this stress range. However, when both confining pressure and temperature are further increased to 120 MPa–140 °C and 140 MPa–160 °C (simulated depths of 6000–7000 m), ductile features become much more pronounced. Taking the 130 MPa–150 °C condition as an example, compared with ambient temperature, the failure mode changes from brittle failure with a single shear crack to bulging deformation accompanied by a dense network of microcracks; the stress–strain curve exhibits more evident pre-peak plastic deformation, and the post-peak stress plateau becomes longer with a more stable stress level. In this case, the pre-peak brittleness index increases from 0.11 to

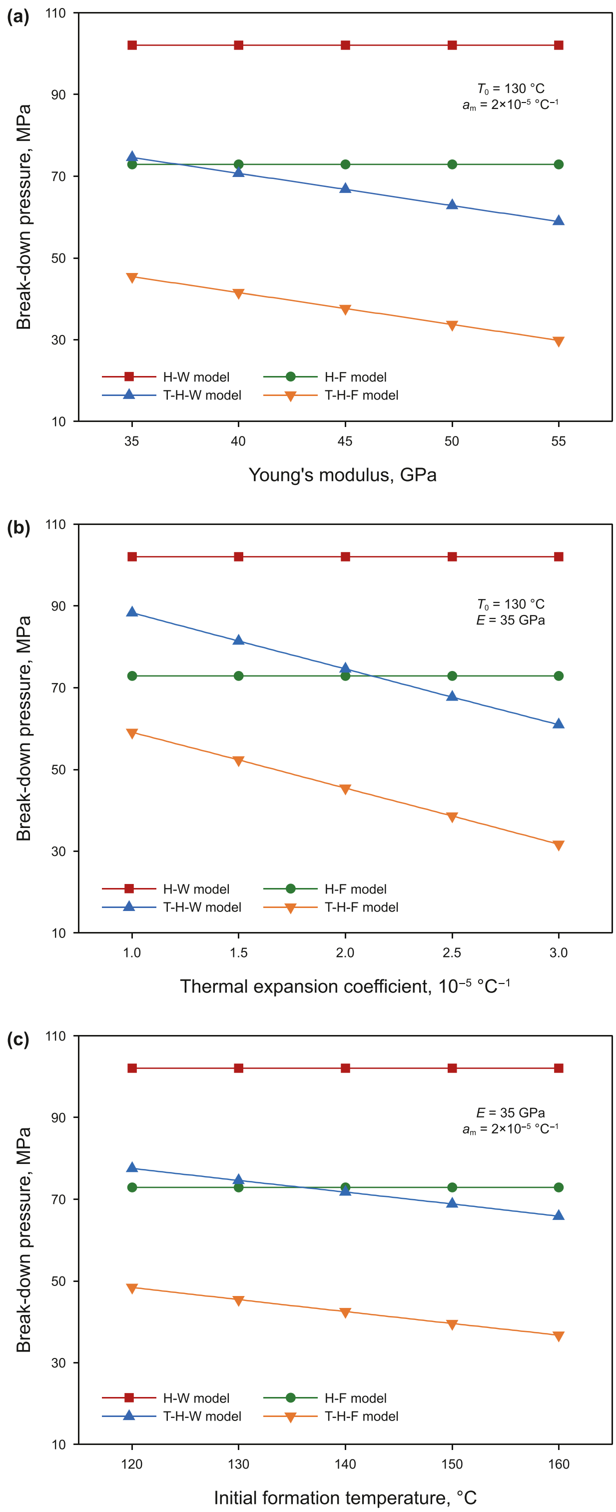

Fig. 11. Parametric sensitivity analysis of breakdown pressure. **(a)** Effect of Young's modulus; **(b)** Effect of thermal expansion coefficient; **(c)** Effect of initial formation temperature.

1.45, increasing by approximately 13 times, and the post-peak brittleness index increases from 2.99 to 4.68, increasing by 57%. These changes demonstrate that, at higher confining pressures, the brittle–ductile transition of ultra-deep rocks becomes highly sensitive to the combined effects of confining pressure and temperature.

Previous studies on sandstone were mostly carried out at relatively low confining pressures and generally suggested that a relatively high temperature (typically >400 °C) is required to trigger a brittle–ductile transition (Ranjith et al., 2012). Under a typical geothermal gradient of 30 °C/km, this implies that reservoir depths greater than 10 km are needed before temperature effects become significant, so traditional understanding has placed more emphasis on the sensitivity of sandstone to confining pressure (Zhang et al., 2024). Recent work, however, has shown that once the confining pressure approaches the brittle–ductile transition regime, the temperature sensitivity of sandstone increases markedly (Jefferd et al., 2021; Liu et al., 2023a; Roy and Singh, 2023). The present results provide a possible explanation for this behavior: under high confining pressure, enhanced lateral confinement suppresses macroscopic unstable fracture propagation. As temperature rises further, the fracture toughness decreases, the number of microcracks increases and their propagation becomes more stable, and the failure mode evolves from localized brittle shear cracking to distributed ductile deformation dominated by dislocation processes and grain-scale cataclastic flow, ultimately leading to a transition in the overall mechanical response.

It is worth noting that triaxial experiments on shale cores by Zhao et al. (2025b) also indicate that a brittle–ductile transition can occur under both 70 MPa–160 °C and 110 MPa–25 °C. In those tests, the failure mode changed from brittle failure along a single macro-shear crack to ductile failure, cataclastic flow failure accompanied by the generation of numerous microcracks, and a pronounced post-peak stress plateau was observed. These features are consistent with the ductile behavior identified in this study under ultra-deep reservoir conditions. Under a typical stress gradient of 0.023 MPa/m, confining pressures of 120–140 MPa correspond to reservoir depths of approximately 5000–6000 m, which fall exactly within the depth interval of greatest interest for ultra-deep hydrocarbon development. Therefore, the brittle–ductile transition and associated temperature sensitivity observed here are likely to have a certain degree of generality.

In summary, for different types of ultra-deep reservoirs, it is beneficial to accurately identify the critical stress state for the brittle–ductile transition and to conduct systematic HPHT mechanical tests within this critical stress range. Such experiments are essential for revealing the temperature sensitivity of the brittle–ductile transition in rocks of different lithologies under critical stress conditions. This, in turn, helps to avoid overestimating rock fracturability in specific reservoir intervals and provides key mechanical parameters for optimizing hydraulic fracturing designs in ultra-deep reservoirs.

4.2. Fracture initiation and propagation mechanisms under ultra-deep reservoir conditions

In ultra-deep reservoirs, the combined influence of rock mechanical properties and in-situ environmental conditions substantially modifies fracture initiation and propagation mechanisms, making hydraulic fracturing optimization more challenging. In this study, true triaxial hydraulic fracturing experiments were conducted on sandstone cubes under different stress state and temperature conditions. The evolution of fracture behavior under deep–ultra-deep reservoir conditions was systematically investigated from three perspectives: injection pressure response, fracture characteristics, and breakdown pressure.

Under deep reservoir conditions, the break-down pressures and fractal dimensions of the fractures at ambient temperature (36 °C) and elevated temperature (90 °C) are nearly identical, indicating that,

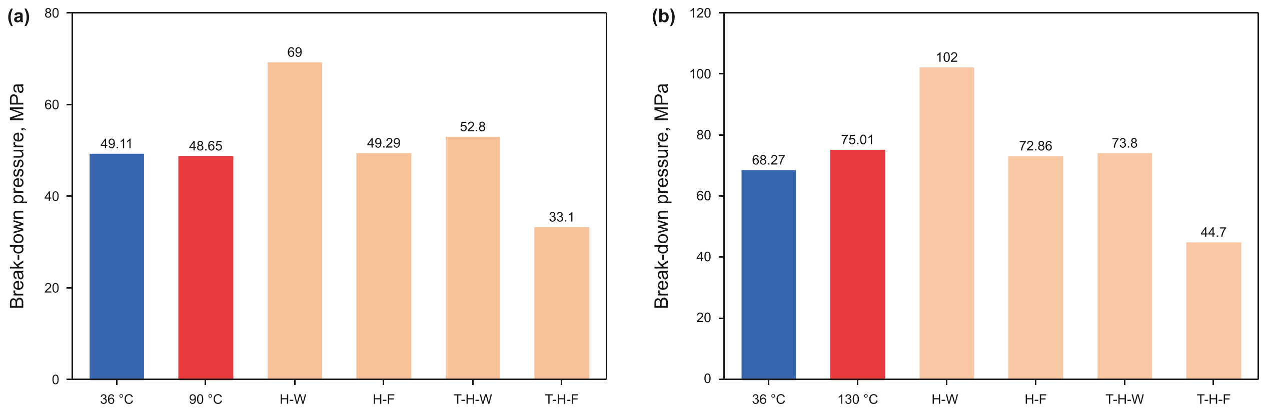

Fig. 12. Comparison of measured results and predicted break-down pressures under high temperature condition. **(a)** Deep reservoir conditions; **(b)** Ultra-deep reservoir conditions. (Blue: ambient temperature experiments; Red: reservoir temperature experiments; Orange: model predictions).

Table 6
Summary table of key parameters and break-down pressure for laboratory and field fracturing tests.

Specimen, #	P_b, MPa	σ_h, MPa	σ_H, MPa	T, °C	E, GPa	ν	σ_t, MPa	Source
5	40.6	35	35	130	45	0.31	9.9	Ju et al. (2025)
6	44.2	35	35	90	45	0.31	9.9	Ju et al. (2025)
7	60.3	37	47	90	13.24	0.31	5.34	Kong et al. (2023)
8	44	41.8	57	90	42.3	0.25	5	Zhang and Wang (2015)
9	78	60	70	90	47.2	0.25	5	Yan et al. (2024)
10	80	57	79	80	35	0.25	5	Cui et al. (2022)
11	93.5	84	126	150	35	0.25	5	Cai et al. (2020)

Table 7
Deviation between test results and predictions of different models under deep reservoir condition.

Specimen, #	Deviation from H-W model, %	Deviation from T-H-W model, %	Deviation from H-F model, %	Deviation from T-H-F model, %
2	41.8	8.5	1.3	−32.0
5	96.8	26.2	−3.9	−74.5
6	80.8	15.9	17.8	−14
7	15.0	−26.3	5.7	−35.6
8	66.8	13.7	11.3	−41.8

Note: The deviation is calculated as (predicted value from different models−experimental value)/experimental value.

Table 8
Deviation between test results and predictions of different models under ultra-deep reservoir condition.

Specimen, #	Deviation from H-W model, %	Deviation from T-H-W model, %	Deviation from H-F model, %	Deviation from T-H-F model, %
4	36.0	−1.6	−2.9	−40.5
9	47.4	0.5	12.5	−34.4
10	21.3	−17.3	−5	−43.6
11	40.1	−4.5	−11.5	−56.0

Note: The deviation is calculated as (predicted value from different models−experimental value)/experimental value.

at relatively low stress state and temperature, both break-down pressure and fracture complexity are only weakly sensitive to temperature. However, the fracture geometries and injection pressure histories differ between the two temperature conditions. Compared with the ambient condition, the high temperature experiment exhibits shorter fracture propagation distances after initiation and more jagged undulations along the fracture surfaces. In addition, the injection pressure during the propagation stage shows a distinct double-peak feature, implying that the fractures undergo episodic arrest and subsequent reactivation at elevated temperature.

Under ultra-deep reservoir conditions, both the break-down pressure and the fractal dimension increase in the high temperature experiment compared with the ambient temperature experiment. This suggests that, at higher stress levels, the influence of temperature on break-down pressure and fracture complexity becomes more pronounced, i.e., the temperature sensitivity is enhanced. Moreover, the differences in injection pressure-time curves between ambient and high temperature conditions are more evident: at high temperature, the injection stage exhibits an initial nonlinear pressurization phase, followed by multiple pressure peaks during fracture propagation, some of which approach the breakdown pressure. We infer that, under HPHT conditions, the enhanced ductility of the rock increases resistance to fracture propagation, so that repeated rebuilding of injection pressure is required to sustain successive episodes of fracture initiation and propagation. This interpretation is consistent with the ductility enhancement observed in the triaxial compression tests.

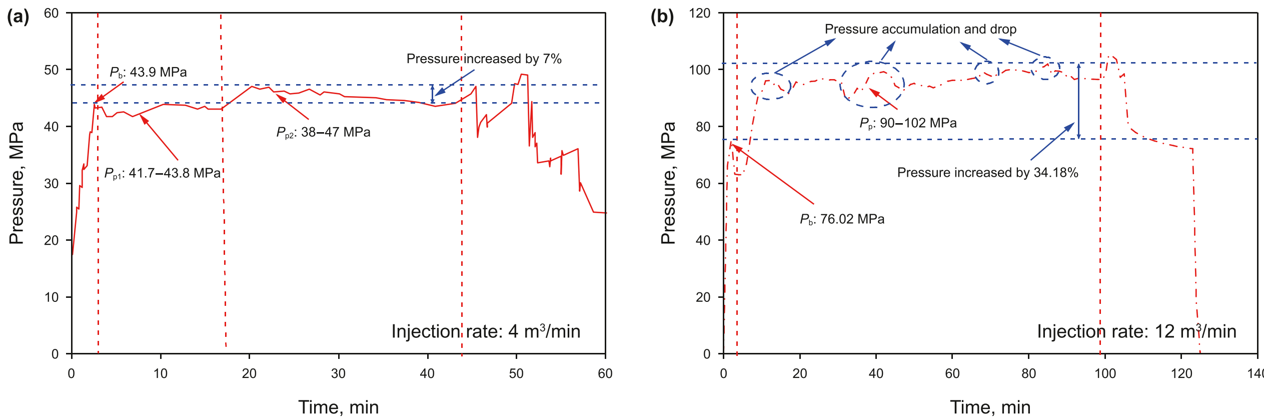

Fig. 13. Pump pressure curve obtained from field fracturing. **(a)** Deep reservoir fracturing curve in the DX184 well (Zhang and Wang, 2015); **(b)** Ultra-deep reservoir fracturing curve in the X5 well.

Field operations exhibit similar injection pressure response characteristics. As shown in Fig. 13, the pumping pressure curves of the deep DX184 well and the ultra-deep X5 well differ markedly: compared with the deep reservoir fracturing, hydraulic fracturing in the ultra-deep reservoir is characterized by a continuously increasing injection pressure, fracture propagation pressures that are close to the breakdown pressure, and pronounced multi-peak oscillations, all indicating stronger resistance to fracture propagation. Therefore, combining the mechanical evolution revealed by triaxial core tests with field-scale injection pressure responses is helpful for identifying the controlling mechanisms of fracture initiation and propagation in ultra-deep reservoirs and for providing theoretical guidance for optimizing fracturing design and operating parameters.

4.3. Applicability of break-down models and study limitations

In ultra-deep reservoir development, accurate prediction of break-down pressure is critical for hydraulic fracturing design and operational safety. In this study, four break-down models are employed to interpret and compare the breakdown pressures obtained from true triaxial hydraulic fracturing experiments under HPHT conditions and from field fracturing operations. The parameter sensitivity analysis and prediction result comparison show that, at relatively low stress state and temperature, the stress perturbation induced by fluid leak-off into the formation plays a dominant role in determining break-down pressure. Under such conditions, the H-F model provides predictions that are closest to the measured values. As stress level and temperature increase, thermally induced stresses associated with fluid–rock temperature difference become progressively more important, while pore compaction in the rock matrix also intensifies. In this regime, the contribution of thermal stress to breakdown pressure becomes significant, and the T-H-W model yields more physically consistent and accurate predictions. It should be noted that all four models assume that fracture initiation is localized at a point on the borehole wall, and they neglect the time-dependent evolution of the temperature field as well as the long-term evolution of rock mechanical properties under HPHT conditions. Therefore, further refinement of break-down pressure models for ultra-deep environments could incorporate transient thermal fields and time-dependent mechanical property evolution on the basis of the existing theoretical framework.

From the sensitivity analysis, E, α_m and T_0 all have a pronounced influence on thermally induced stresses and hence on predicted break-down pressure. To assess the applicability of the adopted models to different ultra-deep reservoir types, we compare representative parameter ranges for typical shale, carbonate and hot dry rock reservoirs (Chen et al., 2025d; He et al., 2023; Wu et al., 2023). The typical E of shale, dolomite and granite cores are about 25–40 GPa, 17–67 GPa and 20–40 GPa, respectively (Tan et al., 2023; Wu et al., 2025; Zhao et al., 2025b). These Young's modulus ranges overlap and are of the same order of magnitude in this study. In the temperature range of 70–300 °C, the α_m of shale, dolomite and granite are approximately 1×10^{-5}–4×10^{-5} °C^{-1}, 2.5×10^{-6}–1.5×10^{-5} °C^{-1} and 1×10^{-5} °C^{-1}, respectively (Gong et al., 2025; Wang et al., 2019; Zhu et al., 2021). Shale therefore have α_m comparable to those of the sandstone tested in this study, whereas dolomite and granite exhibits significantly lower α_m. Regarding reservoir temperature, ultra-deep shale and carbonate reservoirs generally exhibit geothermal gradients of ~30 °C/km, while HDR reservoirs often have much higher gradients, commonly reaching 60 °C/km or more (Li et al., 2024; Zhang et al., 2024; Xiong et al., 2025). Taken together, the similarity in parameter magnitudes and sensitivities suggests that the break-down pressure models used here have good potential for extension to ultra-deep shale and carbonate reservoirs. However, their applicability to HDR reservoirs with substantially higher geothermal gradients and markedly lower α_m should be evaluated more cautiously in conjunction with field applications.

It should also be emphasized that, due to the extremely limited and valuable nature of ultra-deep cores, only one specimen was tested for each loading condition in this work. To maximize the representativeness and comparability of the results, core samples were taken from closely spaced depth intervals, and only structurally intact standard specimens without obvious defects were used for testing. According to previous studies, this sampling and testing strategy yields results that are sufficiently robust to the reliability of the present interpretations of brittle–ductile transition behavior in ultra-deep cores and the associated mechanistic insights (Hou et al., 2017a; Liu et al., 2020). Nevertheless, we fully recognize the limitation imposed by the restricted number of specimens. In future work, it will be necessary to obtain more cores from deep and ultra-deep intervals and to conduct additional triaxial compression and hydraulic fracturing tests over a broader HPHT range, with particular emphasis on the brittle–ductile transition window. Such data will help to further refine the evolution laws of rock mechanical properties in ultra-deep reservoirs and provide a more systematic and comprehensive experimental basis for the optimization and calibration of break-down models.

5. Conclusion

In this study, triaxial compression tests on ultra-deep core samples and true triaxial hydraulic fracturing experiments on sandstone cubes were conducted under high pressure and high temperature conditions. The main conclusions are presented as follows.

(1) Under the condition of elevated confining pressures and temperatures, the failure mode evolves from brittle failure with shear cracks to ductile deformation involving numerous distributed microcracks. There is a marked enhancement of both pre-peak and post-peak ductility, which leads to significant changes in Young's modulus, peak strain, and peak strength.
(2) Break-down pressure increases and fracture propagation resistance strengthens with higher stress levels and temperatures. Hydraulic fractures tend to exhibit an intermittent "initiation–arrest–reinitiation" propagation mode, which is difficult to form an effective fracture network.
(3) Four break-down models were employed to systematically compare break-down pressures under different stress states and temperature conditions. For ultra-deep reservoirs at depths greater than 5000 m, thermally induced stresses arising from temperature differences should be incorporated into break-down models, and the T-H-W model outperforms the H-W and H-F models in terms of both predictive accuracy and physical plausibility.

CRediT authorship contribution statement

Zi-Xi Jiao: Writing – original draft, Visualization, Methodology, Formal analysis, Data curation. **Hai-Yan Zhu:** Supervision, Project administration, Methodology, Funding acquisition. **Peng Zhao:** Writing – review & editing, Visualization, Funding acquisition, Data curation. **Shi-Jie Chen:** Writing – review & editing, Methodology. **Xian-Bo Meng:** Resources, Project administration, Data curation. **Shou-Wei Zhou:** Methodology, Conceptualization. **Jun Zhou:** Writing – review & editing.

Declaration of competing interest

The authors declare that they have no known competing financial interests or personal relationships that could have appeared to influence the work reported in this paper.

Acknowledgement

This study was financially supported by the National Natural Science Foundation of China (No. 52374004) and the Natural Science Foundation of Sichuan Province (No. 2025ZNSFSC0371).

References

Ai, C., Zhang, J., Li, Y.W., Zeng, J., Yang, X.L., Wang, J.G., 2016. Estimation criteria for rock brittleness based on energy analysis during the rupturing process. Rock Mech. Rock Eng. 49, 4681–4698. https://doi.org/10.1007/s00603-016-1078-x.

Barbot, S., Zhang, L., 2023. Constitutive behavior of olivine gouge across the brittle-ductile transition. Geophys. Res. Lett. 50, e2023GL105916. https://doi.org/10.1029/2023GL105916.

Cai, J.J., Liang, F., Zhan, T.H., Wang, L.J., Tang, Q.S., Deng, Z., Gan, X.F., 2020. Application of dynamic and static data in recognition of Sinian carbonate reservoir types in the Moxi-Gaoshiti areas, Sichuan Basin. Nat. Gas Geosci. 31 (1), 132–142. https://doi.org/10.11764/j.issn.1672-1926.2019.05.011 (in Chinese).

Chen, S.J., Zhao, P., Jiao, Z.X., Zhou, J., Tang, X.H., 2025a. Time-lag characteristics and strength evolution of rock failure under unloading conditions. Phys. Fluids 37, 054106. https://doi.org/10.1063/5.0270409.

Chen, S.J., Zhu, H.Y., Zhao, P., Jiao, Z.X., McLennan, J.D., Zhou, J., 2025b. Exploratory study on regulation of thermal short-circuiting in multi-well enhanced geothermal systems. Rock Mech. Rock Eng. 2025, 1–18. https://doi.org/10.1007/s00603-025-05168-2.

Chen, S.J., Zhu, H.Y., Zhao, P., Wang, Y.Y., Song, R.C., Zuo, Y.H., Shi, Y., Zhou, T., 2025c. Influence of fracture network characteristics of hot dry rock on heat extraction performance: a numerical simulation study. Geoenergy Sci. Eng. 245, 213523. https://doi.org/10.1016/j.geoen.2024.213523.

Chen, S.J., Zhou, J., Que, Y., Zhao, P., Hu, Z.M., Wang, Y.J., Jiao, Z.X., 2025d. The effect of in situ stress variation on heat extraction from enhanced geothermal systems (EGS): an experimental study. Phys. Fluids 37, 116609. https://doi.org/10.1063/5.0303456.

Cheng, G.X., Jiang, B., Li, F.L., Li, M., Song, Y., Hou, C.L., 2023. Experimental study on brittle-to-ductile transition mechanism of lower Silurian organic-rich shale in south China. Int. J. Rock Mech. Min. Sci. 170, 105543. https://doi.org/10.1016/j.ijrmms.2023.105543.

Cui, E.L., Tang, H.Y., Yang, K., Wang, Y.W., Sun, Z.L., Zhang, L.H., Teng, H., 2022. Research on analysis method of fracturing pump injection curve in tight conglomerate reservoir. In: the 2022 IFEDC, International Field Exploration and Development Conference, Xi An, IFEDC-202211835 (in Chinese).

Davarpanah, S.M., Sharghi, M., Narimani, S., Török, Á., Vásárhelyi, B., 2023. Brittle-ductile transition stress of different rock types and its relationship with uniaxial compressive strength and Hoek–Brown material constant (mi). Sci. Rep. 13, 1186. https://doi.org/10.1038/s41598-023-28513-3.

Deng, J.G., Liu, Y., Yu, B.H., He, B.S., Guo, Y.B., Li, B., 2009. Formation fracture pressure prediction method in high temperature and high pressure formations. Petrol. Drill. Technol. 37 (5), 43–46. https://doi.org/10.3969/j.issn.1001-0890.2009.05.010 (in Chinese).

French, M.E., Zhu, W.L., Xiao, X.H., Evans, B., Prior, D.J., 2022. Thermally enhanced water weakening of the Solnhofen limestone. J. Geophys. Res. Solid Earth 127, e2021JB022742. https://doi.org/10.1029/2021JB022742.

Gabova, A., Chekhonin, E., Popov, Y., Savelev, E., Romushkevich, R., Popov, E., Kozlova, E., 2020. Experimental investigation of thermal expansion of organic-rich shales. Int. J. Rock Mech. Min. Sci. 132, 104398. https://doi.org/10.1016/j.ijrmms.2020.104398.

Gong, J.J., Liu, X., Yao, Y.L., Hong, B.N., 2025. On the change of linear expansion coefficient of red sandstone based on microstructure experiment. J. Hunan Univ. Sci. Technol. (Nat. Sci. Ed.) 40 (1), 15–21. https://doi.org/10.13582/j.cnki.1672-9102.2025.01.003 (in Chinese).

Guo, X.S., Hu, D.F., Li, Y.P., Duan, J.B., Ji, C.H., Duan, H., 2018. Discovery and theoretical and technical innovations of Yuanba gas field in Sichuan Basin, SW China. Petrol. Explor. Dev. 45 (1), 15–28. https://doi.org/10.1016/S1876-3804(18)30002-8.

Haimson, B., Fairhurst, C., 1969. Hydraulic fracturing in porous-permeable materials. J. Petrol. Technol. 21 (7), 811–817. https://doi.org/10.2118/2354-PA.

He, Q., He, B., Li, F.X., Shi, A.P., Chen, J., Xie, L.Z., Ning, W.X., 2021. Fractal characterization of complex hydraulic fractures in oil shale via topology. Energies 14 (4), 1123. https://doi.org/10.3390/en14041123.

He, X., Chen, G.S., Wu, J.F., Liu, Y., Wu, S., Zhang, J., Zhang, X.T., 2023. Deep shale gas exploration and development in the southern Sichuan Basin: new progress and challenges. Nat. Gas. Ind. B. 10 (1), 32–43. https://doi.org/10.1016/j.ngib.2023.01.007.

Herrmann, J., Rybacki, E., Sone, H., Dresen, G., 2018. Deformation experiments on bowland and posidonia shale—Part I: strength and Young's modulus at ambient and in situ pc–T conditions. Rock Mech. Rock Eng. 51, 3645–3666. https://doi.org/10.1007/s00603-018-1572-4.

Hou, B., Diao, C., Li, D., 2017a. An experimental investigation of geomechanical properties of deep tight gas reservoirs. J. Nat. Gas Sci. Eng. 47, 22–33. https://doi.org/10.1016/j.jngse.2017.09.004.

Hou, P., Gao, F., Ju, Y., Yang, Y.G., Gao, Y.N., Liu, J., 2017b. Effect of water and nitrogen fracturing fluids on initiation and extension of fracture in hydraulic fracturing of porous rock. J. Nat. Gas Sci. Eng. 45, 38–52. https://doi.org/10.1016/j.jngse.2017.05.012.

Hubbert, M.K., Willis, D.G., 1957. Mechanics of hydraulic fracturing. Pet. Trans. AIME 210 (1), 153–168. https://doi.org/10.2118/686-G.

Jefferd, M., Brantut, N., Meredith, P.G., Mithchell, T.M., Plümper, O., 2021. Compactive deformation of sandstone under crustal pressure and temperature conditions. J. Geophys. Res. Solid Earth 126, e2020JB020202. https://doi.org/10.1029/2020JB020202.

Jia, C.Z., 2023. Key scientific and technological problems of petroleum exploration and development in deep and ultra-deep formation. J. China Univ. Pet. (Ed. Nat. Sci.) 47 (5), 1–12. https://doi.org/10.3969/j.issn.1673-5005.2023.05.001 (in Chinese).

Ju, Y., Guo, F., Zhang, G.L., Fu, G.M., Wu, G.J., Liu, P., 2025. Effects of high temperatures and horizontal geostress differences on hydraulic fracture propagation in tight sandstones: an experimental investigation. Geoenergy Sci. Eng. 246, 213644. https://doi.org/10.1016/j.geoen.2025.213644.

Kong, M.W., Zhang, Z.P., Zhao, C.Y., Chen, H.S., Ma, X.F., Zou, Y.S., 2021. Rock mechanical properties and breakdown pressure of high-temperature and high-pressure reservoirs in the southern margin of Junggar Basin. Geofluids 2021, 1116136. https://doi.org/10.1155/2021/1116136.

Kong, X.W., Huang, H., Xie, G.Y., Yan, R.T., Xu, H.X., Li, S., 2023. Experimental study on equilibrium initiation and extension of multiple clusters of fractures based on true triaxial physical simulation. J. Nat. Gas Geosci. 8, 349–362. https://doi.org/10.1016/j.jnggs.2023.08.003.

Lei, Q., Xu, Y., Yang, Z.W., Cai, B., Wang, X., Zhou, L., Liu, H.F., Xu, M.J., Wang, L.W., Li, S., 2021. Progress and development directions of stimulation techniques for ultra-deep oil and gas reservoirs. Petrol. Explor. Dev. 48 (1), 221–231. https://doi.org/10.1016/S1876-3804(21)60018-6.

Lei, Q., Yang, Z.W., Wang, D.W., Liu, H.T., Guan, B.S., Cai, B., Fu, H.F., Liu, Z.L., Duan, Y.Y., Liang, T.C., Ma, Z.Y., 2022. Techniques for improving fracture-controlled stimulated reservoir volume in ultra-deep fractured tight reservoirs: a case study of Kuqa piedmont clastic reservoirs, Tarim Basin, NW China. Petrol. Explor. Dev. 49 (5), 1169–1184. https://doi.org/10.1016/S1876-3804(22)60341-0.

Li, G.X., Lei, Z.D., Dong, W.H., Wang, H.Y., Zheng, X.F., Tan, J., 2022. Progress, challenges and prospects of unconventional oil and gas development of CNPC. China Pet. Expl. 27 (1), 1–11. http://www.cped.cn/EN/10.3969/j.issn.1672-7703.2022.01.001.

Li, L., Ma, S.M., Liu, X., Liu, J., Lu, Y., Zhao, P., Kassabi, N., Hamdi, E., Elsworth, D., 2024. Coal measure gas resources matter in China: review, challenges, and perspective. Phys. Fluids 36, 071301. https://doi.org/10.1063/5.0218328.

Li, L., Ben Abdallah, K., Hamdi, E., Hou, B., Cui, Z., Elsworth, D., Liu, J., 2026. CO_2-enhanced multiphase flow in heterogenous coal measures: thermal–hydraulic–mechanic (THM) model for enhancing gas co-production with CO_2 geo-sequestration. Fuel 407, 137479. https://doi.org/10.1016/j.fuel.2025.137479.

Li, N., Zhang, S.C., Wang, H.B., Ma, X.F., Zou, Y.S., Zhou, T., 2021. Effect of thermal shock on laboratory hydraulic fracturing in Laizhou granite: an experimental study. Eng. Fract. Mech. 248, 107741. https://doi.org/10.1016/j.engfracmech.2021.107741.

Li, S.G., Deng, J.G., Wei, B.H., Yu, L.J., 2005. Formation fracturing pressure calculation in high temperature wells. Chin. J. Rock Mech. Eng. 24, 5669–5673. http://www.rockmech.org/EN/Y2005/V24/IS2/5669.

Liu, S.L., Chen, H.R., Yuan, S.S., Zhu, Q.Z., 2020. Experimental investigation and micromechanical modeling of the brittle-ductile transition behaviors in low-porosity sandstone. Int. J. Mech. Sci. 179, 105654. https://doi.org/10.1016/j.ijmecsci.2020.105654.

Liu, J.X., Xu, H.W., Li, J.R., Asce, S.M., Tang, W., Liu, W., Hu, Q.J., Heng, S., 2023a. Thermal effect on the compaction behavior of tight shale by uniaxial strain test. J. Eng. Mech. 149 (7), 04023039. https://doi.org/10.1061/JENMDT.EMENG-6935.

Liu, J.Y., Zhao, J.M., Qin, S.Y., Zhang, N.L., Ren, D.F., Luo, Z.F., Xie, Y.Z., 2023b. Research and application of acid fracturing stimulation mechanism in ultra-deep subsalt dolomite reservoir in Tarim Basin. J. Pet. Explor. Prod. Technol. 13, 877–889. https://doi.org/10.1007/s13202-022-01578-y.

Ma, Y.S., Cai, X.Y., Li, M.W., Li, H.L., Zhu, D.Y., Qiu, N.S., Pang, X.Q., Zeng, D.Q., Kang, Z.J., Ma, A.L., Shi, K.B., Zhang, J.T., 2024. Research advances on the mechanisms of reservoir formation and hydrocarbon accumulation and the oil and gas development methods of deep and ultra-deep marine carbonates. Petrol. Explor. Dev. 51 (4), 795–812. https://doi.org/10.1016/S1876-3804(24)60507-0.

Meng, F.Z., Wong, L.N.Y., Zhou, H., 2021. Rock brittleness indices and their applications to different fields of rock engineering: a review. J. Rock Mech. Geotech. Eng. 13, 221–247. https://doi.org/10.1016/j.jrmge.2020.06.008.

Meng, Y., Jin, J., Gao, C.L., Li, J., Liu, M., Liu, K., Wang, K., Ren, Y., Deng, Y., 2022. Characteristics and physical property preservation mechanism of Cretaceous deep reservoir in western segment of southern margin of Junggar Basin. Nat. Gas Geosci. 33 (2), 218–232. https://doi.org/10.11764/j.issn.1672-1926.2021.07.013 (in Chinese).

Qin, Q.L., Zhou, K., Wei, B., Du, Q.J., Liu, Y.G., Li, X., Hou, J., 2024. Experimental and simulation study on deep reservoir fracturing technology: a review and future perspectives. Geoenergy Sci. Eng. 242, 213209. https://doi.org/10.1016/j.geoen.2024.213209.

Ranjith, P.G., Daniel, R.V., Bai, J.C., Samintha, A.P., 2012. Transformation plasticity and the effect of temperature on the mechanical behaviour of Hawkesbury sandstone at atmospheric pressure. Eng. Geol. 151, 120–127. https://doi.org/10.1016/j.enggeo.2012.09.007.

Roy, D.G., Singh, T.N., 2023. Effect of heat-treatment on the pure- and mixed-mode fracture properties of a homogeneous sandstone. Geom. Energy Environ. 33, 100430. https://doi.org/10.1016/j.gete.2022.100430.

Sampath, K.H.S.M., Perera, M.S.A., Ranjith, P.G., 2018. Theoretical overview of hydraulic fracturing break-down pressure. J. Nat. Gas Sci. Eng. 58, 251–265. https://doi.org/10.1016/j.jngse.2018.08.012.

Segall, P., Simpson, C., 1986. Nucleation of ductile shear zones on dilatant fractures. Geology 14 (1), 56–59. https://doi.org/10.1130/0091-7613(1986)14<56:NODSZO>2.0.CO;2.

Stephens, G., Voight, B., 1982. Hydraulic fracturing theory for conditions of thermal stress. Int. J. Mech. Min. Sci. Geomech. Abstr. 19 (6), 279–284. https://doi.org/10.1016/0148-9062(82)91364-X.

Sun, L.D., Ma, F., Jiang, H., Jing, Z.H., Yu, H., Gao, B., Dong, H.X., Zeng, F.D., Shan, Y.P., Yang, Y.C., 2025. Progress and assessment of onshore oil and gas exploration and development in deep to ultra-deep formations. Deep Earth Energy Sci. Technol. 1 (1), 14–26 (in Chinese).

Sun, J., Qi, H.Y., Xue, J.J., Zhang, Q., Chang, Q.S., 2023. Characteristics and controlling factors of deep and ultra deep tight conglomerate reservoirs in the Junggar Basin. Nat. Gas. Ind. 43 (8), 26–37. https://doi.org/10.3787/j.issn.1000-0976.2023.08.003 (in Chinese).

Tan, X.F., Zhang, Q., Zhan, Q.S., Li, S.H., Jiang, H.Y., Zhang, F., 2023. Study on rock mechanical properties of hot-dry rock reservoir under high temperature. Drill. Eng. 50 (4), 110–117. https://doi.org/10.12143/j.ztgc.2023.04.015 (in Chinese).

Tarasov, B., Potvin, Y., 2013. Universal criteria for rock brittleness estimation under triaxial compression. Int. J. Rock Mech. Min. Sci. 59, 57–69. https://doi.org/10.1016/j.ijrmms.2012.12.011.

Ulusay, R., Hudson, J.A., 2007. The complete ISRM suggested methods for rock characterization, testing and monitoring: 1974–2006. Environ. Eng. Geosci. 15, 47–48. https://doi.org/10.2113/gseegeosci.15.1.47.

Wang, X., Xu, X.X., Ye, Y., Wang, C., Liu, D., Shi, X.C., Wang, S., Zhu, X., 2019. In-situ high-temperature XRD and FTIR for calcite, dolomite and magnesite: anharmonic contribution to the thermodynamic properties. J. Earth Sci. 30, 964–976. https://doi.org/10.1007/s12583-019-1236-7.

Wang, Y.J., Sun, Y.H., Yang, S.Y., Wu, S.H., Liu, H., Tong, M., Lyu, H.Y., 2022. Saturation evaluation of microporous low resistivity carbonate oil pays in Rub Al Khali Basin in the Middle East. Petrol. Explor. Dev. 49 (1), 94–106. https://doi.org/10.1016/S1876-3804(22)60007-7.

Wen, D.S., Wang, X.Z., Ding, H.Z., Fu, Z.B., 2023. Estimation of crack initiation stress based on axial crack strain expansion rate. Rock Mech. Rock Eng. 56, 1025–1041. https://doi.org/10.1007/s00603-022-03113-1.

Wu, F.P., Li, D., Fan, X.Z., Liu, J., Li, X.J., 2020. Analytical interpretation of hydraulic fracturing initiation pressure and breakdown pressure. J. Nat. Gas Sci. Eng. 76, 103185. https://doi.org/10.1016/j.jngse.2020.103185.

Wu, K.L., Zhu, Q.Y., Chen, Z.X., Li, J., Feng, D., Wang, M.Y., Guo, S.Q., Guo, Y.C., 2023. Microscopic gas displacement efficiency of enhanced gas recovery in carbonate gas reservoirs with edge and bottom water. Nat. Gas. Ind. B. 10 (4), 372–382. https://doi.org/10.1016/j.ngib.2023.07.006.

Wu, S.J., Wu, J., Fan, T.L., Ding, M., Lü, K.D., Li, G.P., Li, Y.P., 2025. Correlation characteristics and genetic mechanisms between lithofacies and mechanical properties of deep carbonate rocks. Petrol. Geol. Exp. 47 (6), 1224–1240. https://doi.org/10.11781/sysydz2025061224 (in Chinese).

Wu, X.Y., Baud, P., Wong, T.F., 2000. Micromechanics of compressive failure and spatial evolution of anisotropic damage in Darley Dale sandstone. Int. J. Rock Mech. Min. Sci. 37, 143–160. https://doi.org/10.1016/S1365-1609(99)00093-3.

Xie, H.P., Gao, M.Z., Fu, C.H., Lu, Y.Q., Yang, M.Q., Hu, J.J., Yang, B.G., 2021. Mechanical behavior of brittle-ductile transition in rocks at different depths. J. China Coal Soc. 46 (3), 701–715. https://doi.org/10.13225/j.cnki.jccs.yt21.0157 (in Chinese).

Xiong, B., Xu, H., Fang, C.H., Li, S.X., Tang, S.L., Wang, S.J., Wu, J.J., Song, X.J., Zhang, L., Wang, J.W., Wei, X.Q., Xin, F.D., Tang, B.N., Long, Y., 2025. Construction and application of favorable target evaluation system for hot dry rock. Petrol. Explor. Dev. 52 (1), 258–271. https://doi.org/10.1016/S1876-3804(25)60019-X.

Yan, J.P., Lai, S.Y., Guo, W., Liao, M.J., Huang, Y., 2024. Application of fracturing construction curve in fracture evaluation of deep shale gas horizontal wells. J. Southwest Petro. Univ. (Sci. Technol. Ed.) 46 (5), 1–18. https://doi.org/10.11885/j.issn.1674-5086.2022.10.18.04 (in Chinese).

Yang, Z., Zou, C.N., 2022. Orderly "symbiotic enrichment" of conventional & unconventional oil and gas——discussion on theory and technology of conventional & unconventional petroleum geology. Acta Geol. Sin. 96 (5), 1635–1653 (in Chinese). https://10.19762/j.cnki.dizhixuebao.2022227.

Yang, H.J., Wang, C.S., Yang, X.Z., Zhang, Z., Guo, X.G., Sun, C.H., Lyu, X.G., Liu, J.L., 2025. Technological progress and scientific significance of the drilling of the ten-thousand-meter ultra-deep well TK1, Tarim Basin, NW China. Petrol. Explor. Dev. 52 (5), 1329–1339. https://doi.org/10.1016/S1876-3804(25)60645-8.

Yong, R., Yang, H.Z., Wu, W., Yang, X., Yang, Y.R., Huang, H.Y., 2025. Controlling factors and exploration potential of shale gas enrichment and high yield in Permian Dalong Formation, northern Sichuan Basin, SW China. Petrol. Explor. Dev. 52 (2), 285–300. https://doi.org/10.1016/S1876-3804(25)60567-2.

Yu, J.J., Li, N.Y., Hui, B., Zhao, W., Li, Y., Kang, J., Hu, P., Chen, Y., 2024. Experimental simulation of fracture propagation and extension in hydraulic fracturing: a state-of-the-art review. Fuel 363, 131021. https://doi.org/10.1016/j.fuel.2024.131021.

Zha, E.S., Duan, H.F., Chi, M.B., Fan, J.L., Hu, J.J., Wu, B.Y., Yu, C., Tong, J.C., 2025. Depth-dependent mechanical–seepage behavior and safety mining distance of the steeply inclined coal mine underground reservoir. Int. J. Min. Sci. Technol. 35, 1341–1355. https://doi.org/10.1016/j.ijmst.2025.07.006.

Zhang, P., Mishra, B., Heasley, K.A., 2015a. Experimental investigation on the influence of high pressure and high temperature on the mechanical properties of deep reservoir rocks. Rock Mech. Rock Eng. 48, 2197–2211. https://doi.org/10.1007/s00603-015-0718-x.

Zhang, D.C., Ranjith, P.G., Perera, M.S.A., 2016. The brittleness indices used in rock mechanics and their application in shale hydraulic fracturing: a review. J. Pet. Sci. Eng. 143, 158–170. https://doi.org/10.1016/j.petrol.2016.02.011.

Zhang, G., Wu, S.C., Guo, P., Zhang, S.H., 2023. Mechanical deformation, acoustic emission characteristics, and microcrack development in porous sandstone during the brittle–ductile transition. Rock Mech. Rock Eng. 56, 9099–9120. https://doi.org/10.1007/s00603-023-03533-7.

Zhang, S.Q., Ben Abdallah, K., Li, L., Hamdi, E., Liu, J., 2025b. Multiphase flow controlled by synergistic injection–production pressure: enabling CO_2 geo-sequestration with additional gas recovery from vertically heterogeneous depleted shale reservoirs. Fuel 398, 135591. https://doi.org/10.1016/j.fuel.2025.135591.

Zhang, K., Liu, X.F., Wang, D.B., Zheng, B., Chen, T.H., Wang, Q., Bai, H., Yao, E.D., Zhou, F.J., 2024. A review of reservoir damage during hydraulic fracturing of deep and ultra-deep reservoirs. Pet. Sci. 21 (1), 384–409. https://doi.org/10.1016/j.petsci.2023.11.017.

Zhang, T., Wang, X.H., 2015. Research and application of proppant slug technology for carboniferous volcanic reservoir in Junggar Basin. Sino-Global Energy 20 (9), 45–48 (in Chinese).
Zhao, J.Z., Ren, L., Lin, C., Lin, R., Hu, D.F., Wu, J.F., Song, Y., Shen, C., Tang, D.J., Jiang, H., 2025a. A review of deep and ultra-deep shale gas fracturing in China: status and directions. Renew. Sustain. Energy Rev. 209, 115111. https://doi.org/10.1016/j.rser.2024.115111.
Zhao, G.K., Guo, Y.T., Yang, C.H., Chang, X., Guo, W.H., Yang, H.Z., 2025b. Effect of temperature and pressure on mechanical behavior of reservoir shales at different depths: implications for deep shale gas extraction. Rock Mech. Rock Eng. 58, 6169–6194. https://doi.org/10.1007/s00603-025-04470-3.
Zhu, H.Y., Deng, J.G., Jin, X.C., Hu, L.B., Luo, B., 2015. Hydraulic fracture initiation and propagation from wellbore with oriented perforation. Rock Mech. Rock Eng. 48, 585–601. https://doi.org/10.1007/s00603-014-0608-7.
Zhu, H.Y., Gong, D., Zhang, B., 2023. A multi-scale geological–engineering sweet spot evaluation method for tight sandstone gas reservoirs. Nat. Gas. Ind. B. 10 (5), 522–532. https://doi.org/10.1016/j.ngib.2023.09.007.
Zhu, H.Y., Jiao, Z.X., Zhao, P., Tang, X.H., Chen, S.J., Tao, L., 2025. Physico-mechanical properties of granite after thermal treatments using different cooling media. J. Rock Mech. Geotech. Eng. 17, 3619–3631. https://doi.org/10.1016/j.jrmge.2024.10.010.
Zhu, Z.X., Wang, C.F., Guan, Z.G., Lei, W.N., 2021. Thermal characteristics of borehole stability drilling in hot dry rock. ACS Omega 6 (29), 19026–19037. https://doi.org/10.1021/acsomega.1c02311.
Zhuang, D.D., Yin, T.B., Li, Q., Wu, Y., Tan, X.S., 2022. Effect of injection flow rate on fracture toughness during hydraulic fracturing of hot dry rock (HDR). Eng. Fract. Mech. 260, 108207. https://doi.org/10.1016/j.engfracmech.2021.108207.